Abstract

Title of dissertation: Dynamics of Elastic Capsules
in Constricted Microfluidic Channels

Sun-Young Park, Doctor of Philosophy, 2013

Thesis directed by: Professor Panagiotis Dimitrakopoulos
Department of Chemical and Biomolecular Engineering

In this dissertation, we investigate computationally the transient dynamics of an elastic capsule in a square microfluidic channel with two different types of constriction, i.e., a square or a rectangular constriction, and compare them with the dynamics owing to a droplet passing.

In the rectangular constricted microchannel, the confinement and expansion dynamics of the fluid flow results in a rich deformation behavior for the capsule, from an elongated shape at the constriction entrance, to a flattened parachute shape at its exit. Larger capsules are shown to take more time to pass the constriction and cause higher additional pressure difference, owing to higher flow blocking. Our work highlights the effects of two different mechanisms for non-tank-treading transient capsule dynamics. The capsule deformation results from the combined effects of the surrounding and inner fluids normal stresses on the soft particles interface, and thus when the capsule viscosity increases, its transient deformation decreases, as for droplets. However, the capsule deformation is not able to create a strong enough inner circulation (owing to restrictions imposed by the material membrane), and thus the viscosity ratio does not affect much the capsule velocity and the additional pressure difference. In addition, the weak inner circulation results in a positive additional pressure difference ΔP^+ even for low viscosity capsules, in direct contrast to low-viscosity droplets which create a negative ΔP^+.

In addition, we focus on the hydrodynamic forces exerted on the rectangular constriction owing to the capsule passing by considering different capsule sizes, flow

rates and viscosity ratios. As the capsule size increases, the forces increase owing to the higher flow blocking. The hydrodynamic forces on the constriction are only weakly affected by the viscosity ratio. For low-viscosity capsules, the additional hydrodynamic forces on the constriction are positive in direct contrast to low-viscosity droplets which create negative additional hydrodynamic forces on the constriction due to their strong inner circulation.

Finally, we investigate the effects of the constriction type for the transient capsule dynamics. In the square constriction, the capsule is more deformed owing to the larger flow changes associated with the smaller cross-section area of this constriction. The higher flow blocking results in an increase of the capsule velocity, the additional pressure difference and the hydrodynamic forces exerted on the constriction owing to the capsule passing.

Our findings suggest that the high cytoplasmatic viscosity, owing to the protein hemoglobin required for oxygen transport, does not affect adversely the motion of non-tank-trading erythrocytes in vascular capillaries.

Dynamics of Elastic Capsules in Constricted Microfluidic Channels

by

Sun-Young Park

Dissertation submitted to the Faculty of the Graduate School of the
University of Maryland, College Park in partial fulfillment
of the requirements for the degree of
Doctor of Philosophy
2013

Advisory Committee:
Professor Panagiotis Dimitrakopoulos, Chair
Professor Helim Aranda-Espinoza
Professor Richard V. Calabrese
Professor Kyu Yong Choi
Professor Srinivasa R. Raghavan

Acknowledgments

I would like to thank my advisor, Professor Panagiotis Dimitrakopoulos for his support and guidance throughout my graduate studies. His expertise and directions made this work successful.

I must also thank the membrers of our research lab, Shugi Kuriakose, Moon Soo Lee and Navadeep Boruah. I would also like to thank my examining committee members, including Professors Kyu Yong Choi, Richard V. Calabrese, Srinivasa R. Raghavan and Helim Aranda-Espinoza. Further, I must acknowledge the Department of Chemical and Biomolecular Engineering at the University of Maryland, College Park.

I would like to thank my parents, Mr. Ki-Seon Park and Mrs. Young-Sook Kang, for their love and support during my graduate studies. I am also thankful to Prof. Hyo Kim and my friends for their help and support.

This work was supported in part by the National Science Foundation and the National Institutes of Health. Most computations were performed on multiprocessor computers provided by the Extreme Science and Engineering Discovery Environment (XSEDE) which is supported by the National Science Foundation.

Contents

List of Tables

List of Figures

List of Abbreviations

α_p	Prestress parameter
$\Delta \boldsymbol{f}$	Surface stress vector
Δt	Time step
λ	Viscosity ratio
λ_α	Stretch ratio
μ	Ambient viscosity
σ	Stress tensor
τ_α^P	Principal tensions ($\alpha = 1, 2$)
τ_{wall}^∞	Undisturbed shear stress
τ^{const}	Shear stress over the constriction
τ	In-plane stress resultant
a	Capsule radius
C	Dimensionless area-dilatation modulus
Ca	Elastic capillary number
G_s	Shearing modulus
G_a	Area-dilatation modulus
h	Gap between the solid particle's surface and the solid wall
F_x	Hydrodynamic force exerted on the microfluidic constriction
F_x^{sh}	Shear force exerted on the microfluidic constriction
F_x^n	Normal force exerted on the microfluidic constriction
F_x^+	Additional hydrodynamic force exerted on the constriction
F_x^{sh+}	Additional shear force exerted on the constriction
F_x^{n+}	Additional normal force exerted on the constriction
ℓ_x	Half-length of the constriction
ℓ_y	Half-width of the constriction
ℓ_z	Half-height of the constriction
L_x	Capsule length
L_y	Capsule width
L_z	Capsule height
$\boldsymbol{n}$	Surface unit normal vector
N_B	Number of basis points for spectral interpolation
N_E	Number of spectral elements
ΔP	Pressure difference
ΔP^0	Pressure difference in the absence of the soft particle
ΔP^+	Additional pressure difference, $\Delta P^+ = \Delta P - \Delta P^0$

ρ	Density
S	Stokeslet solution for the velocity
S_{const}	Constriction surface area
T	Stokeslet solution for the stress
$\boldsymbol{u}$	Velocity
$\boldsymbol{u}^{\infty}$	Undisturbed velocity
$\mathcal{U}$	Average undisturbed velocity in a microchannel

Chapter 1: Introduction

In this dissertation, we study the interfacial dynamics of artificial or elastic capsules in viscous flows. A capsule is a fluid volume enclosed by an elastic membrane. Capsules have seen an increased interest during the last few decades due to their numerous engineering and biomedical applications [55, 58]. Here, the study of the motion and deformation of capsules and biological cells in microfluidic channels is motivated by a wide range of applications including drug delivery, cell sorting and cell characterization devices [1, 2, 6, 12, 26, 68], fabrication of microparticles and microcapsules with desirable properties [13, 33, 65], determination of membrane properties [42, 61], and of course its similarity to blood flow in vascular capillaries [55].

Therefore, studying the dynamics of soft particles in confined solid ducts, such as microfluidic channels and blood microvessels, provides useful information on the utilization of these particles in chemical, pharmaceutical and physiological processes. For example, understanding the stability of soft particle shapes provides helpful insight on the hydrodynamic aggregation and the effective viscosity of suspensions [17]. The deformation of artificial capsules in microchannels is directly associated with drug delivery, cell sorting and cell characterization [1, 2]. Further-

more, the deformability of red blood cells plays a pivotal role in the oxygen and carbon dioxide exchange between the microcirculation and the body tissues [55], and helps identifying the effects of blood disorders and diseases [6, 25, 68]. Studying the motion of capsules in micro-constrictions is further motivated by its similarity to the erythrocyte motion over endothelial cells and adherent leukocytes in vascular capillary vessels as well as other attached protuberances of biological nature such as those formed during cancer cell metastasis and biofilm formation [28, 72, 77, 78].

The deformation of capsules and biological cells in microfuidic channels is determined by the nonlinear coupling of the deforming hydrodynamic forces with the restoring interfacial forces of the particle membrane. Since the latter forces depend on the type of the soft-particle interface, this suggests that different soft particles (such as droplets, capsules, vesicles and erythrocytes) may obtain quite different shapes as they travel in a microfuidic device. [10, 17, 38].

The motion of elastic capsules in cylindrical microchannels has been studied both experimentally and computationally. Leyrat-Maurin and Barthès-Biesel [45] studied the motion of a single capsule flowing through a hyperbolic pore. They calculated the capsule velocity and the recovery energy for varying flow rates when the capsule passees through the pore. Quèguiner and Barthès-Biesel [62] used a boundary integral method to study the flow of capsules into a hyperbolic constricted cylindrical channel. They studied the effects of capsule size, geometry and membrane properties. Risso and coworkers [63] studied experimentally the motion of artificial capsules in a narrow tube and compared their findings with computational results. The deformed capsules are affected by the capillary number and the relative capsule

size to tube size. Lefebvre and Barthes-Biesel [43] investigated the effects of membrane prestress and various constitutive laws at steady state. They found that the back curvature is dependent on pre-inflation. They concluded that the pre-inflation accounted for the difference between the experimental data and numerical results of earlier studies [62, 63]. She *et al.* [67] investigate experimentally the deformation of multilayered microcapsules and recovery after passing through a cylindrical microchannel for varying the layer thickness of the multilayered microcapsule and the capsule size.

Doddi and Bagchi [22] investigated the lateral migration of a neo-Hookean capsule in a Poiseuille flow in a channel at low-Reynolds number. They found that all capsules moved away from the wall toward the center of flow. Coupier and coworkers [16] studied non-inertial lateral migration of a vesicle in a bounded Poiseuille flow experimentally and numerically. The migration velocity is associated with a gap between the walls and the capsule surface, the capsule size and the flow velocity. Kaoui and coworkers [34] studied the lateral migration of a vesicle in an unbounded Poseuille flow without viscosity contrast between the exterior and interior fluids. The interaction between the nonlinear character of the Poiseuille flow and the vesicle deformation causes a cross-streamline migration of vesicles toward the center of flow center line.

Recent studies have also focused on capsule dynamics in noncylindrical microfluidic channel. Zhu and coworkers [81] studied computationally the motion of soft 2D microcapsules through a constriction channel. They probed the effects of the capsule rigidity and interaction with the pillars on the capsule velocity. Arata

and Alexeev [4] studied the transient dynamics of the capsule in a microfluid channel decorated with stiff ridges protruding from the opposite walls. They investigated the effects of the capillary number and the ridge gap on the lateral migration rate of the capsule. In addition, they calculated the strain of the capsule surface and fluid velocity using three-dimensional computer simulations. Mao and Alexeev [46] computed the stream velocity distribution near protuberances from the opposite channel walls as microparticles passing for varying Reynolds number. They also investigated the capsule migration as the capsule passed protuberances. Fiddes and coworkers [26] conducted experiments to study the effects of confinement (i.e. interactions between the microcapsule and the solid walls) on the microcapsule's velocity and its deformation. Leclerc and coworkers [42] conducted experiments to investigate the transient behavior of ovalbumin microcapsules passing through a square convergent-divergent microchannel. They investigated the relaxation time of microcapsules at the exit of pores according to capsule sizes, velocity and cross-section area.

Kuriakose and Dimitrakopoulos [37] studied the steady-state motion of an elastic capsule in a square channel and compared their results with those in a cylindrical tube. They considered slightly over-inflated elastic capsules following the Skalak *et al.* constitutive law. They derived power laws and theoretical analysis for the capsule motion in a square channel and in a cylindrical tube. Recently, the same authors investigated the deformation of elastic capsules at steady-state in a rectangular channel for varying capsule size, capillary number and the membrane hardness [38]. In addition, they compared their results with those for droplets

passing.

In biomedical fields, the motion of erythrocytes has been studied both experimentally and computationally in capillary blood vessels or microfluidic devices. Skalak and Branemark [69] observed shapes of red blood cells in capillary vessels. Flowing red blood cells have parachute or umbrella shapes. Shelby *et al.* [68] demonstrated experimentally the deformation and shape recovery time of malaria-infected erythrocytes to verify the effects of stiffness of membrane. Through varying channel widths, they compared the motion of uninfected cells and infected cell. The more stiff cells are easily blocked. Recovery time of infected cell is also significantly longer than that for uninfected cell. It means that the membrane rigidity and internal viscosity are crucial factors for determining the cell motion. Abkarian, Faivre and Stone [1] investigated experimentally the motion of erythrocytes in a constricted microchannel. They measured the pressure drop variation associated with the motion of single and multiple erythrocytes and leukocytes in the channel. Secomb and coworkers [64] investigated the axisymmetric erythrocyte motion in a nonuniform capillary numerically. According to their results, the blood resistance in a wavy capillary is approximately four times higher than in a cylindrical vessel. Noguchi and Gompper [49] focused on the transient motion of red blood cells and vesicles in capillary flows by using a three-dimensional mesoscopic method. The flow velocity affects the transient motion of the red blood cells and vesicles. In addition, the bending rigidity and the shear modulus of the membrane affects the shape transitions. Pozrikidis [59] studied the axisymmetric motion of a file of red blood cells in a cylindrical vessel. The author computed the motion of cells using a boundary

integral methods for axisymmetric Stokes flow. He studied the effects of the mean velocity, the hematocrit and the capillary diameters on the motion of cells. Sun and Munn [73] developed a 2D lattice Boltzmann method to describe the motion of multiple cells in blood flow. They determined the flow resistance at various hematocrits and vessel diameters. In addition, they determined the increase of resistance in flow owing to leukocytes rolling or adhesion. Bagchi [7] studied the migration of a single erythrocyte and multiple erythrocytes in a two-dimensional rectangular channel, and found that the migration velocity was influenced by the deformability and their position of erythrocytes in a channel. Tomaiuolo *et al.* [74] reported on the red blood cells suspension in microcapillaries. They obtained the cell velocity and pressure gradient according to the cell area. To verify the cell deformation, they compared their experimental results with numerical simulation [59]. Isfahani and Freund [32] calculated studied the forces on the wall-adhered leukocyte as the red blood cells pass by corresponding homogeneous blood models. They focused on the effects on the leukocyte geometry and hematocrit on the forces exerted on the adherent leukocyte in a microvessel.

In this dissertation, we consider capsules made of elastic membranes with shearing and area-dilatation resistance but negligible bending resistance. Experimental results of biocompatible alginate capsules [11] and synthetic polysiloxane [31] are in very good agreement with the theoretical results without considering bending resistance. In addition, this model can be extended to the human red blood cells where hemoglobin solution is enclosed by the multi-layer membrane. In this dissertation, we investigate in detail the transient dynamics of elastic capsules in

the microfluidic constricted channel (i.e., a rectangular or square constriction). The motivation of this research is to study the capsule deformation, flow properties and forces exerted on the constriction channel. The deformed shape of capsules is important in several microfluidic processes including cell sorting, filtration system and fabrication [2, 6, 26, 65]. In addition, the study of the deformable red blood cells is important to understand the cell motion in the capillary blood vessels. To a great extend, the study applies to the diagnosis of blood cell diseases. Therefore, in this dissertation, we investigate the transient capsule motion for different constriction types for both small-to-moderate capsules compare to the height of the constriction.

In summary, the present dissertation has three main goals: (a) to investigate the transient dynamics of an elastic capsule when it passes through a microfluidic constricted channel, (b) to study the hydrodynamic forces exerted on the constriction as the capsule passes through the constriction, and (c) to compare the capsule and a droplet transient motion in the microfluidic constricted channel.

In chapter 2, we introduce the mathematical formulation of the problem including the governing equations and boundary integral equations. We describe the three-dimensional Membrane Spectral Boundary Element (MBE) method. We utilize in our computations. The details of the channel geometry and the physical parameters of the problem are defined in this chapter.

In chapter 3, we investigate the motion of an elastic capsule in a rectangular constricted microchannel for varying flow rates, capsule sizes and viscosity ratios. We analyze in detail the transient motion of the capsule, the capsule deformation, its velocity and additional pressure differences when it passes through the constric-

tion. In addition, we compare the transient motion of capsules and droplets in the rectangular constriction.

In chapter 4, we study the hydrodynamic forces exerted on the rectangular constriction as the capsule passes through the constriction. We focus on the effects of the flow rate, capsule size and the viscosity ratio on these forces. The shear and normal forces are also considered. Furthermore, we also compute the forces exerted on the rectangular constriction owing to droplet passing and compare them with those owing to the capsule passing in the constriction.

In chapter 5, we investigate the effects of the constriction types on the transient motion of the capsule. Following our invesitgation in chapter 3, we focus on the transient motion of the capsule, including the capsule deformation, velocity, pressure gradient and forces in the square constriction. In addition, we compare the capsule motion in the square constriction with that presented in chapter 3 and 4 in the rectangular constriction. A conclusion of our study are presented in chapter 6.

Chapter 2: Mathematical formulation

In this chapter, we describe the mathematical formulation and the numerical algorithm used in this dissertation. We study the dynamics of capsules flowing along the centerline of a constricted microfluidic channel. The study is characterized by small length scales resulting in low-Reynolds number flows and the Navier-Stokes equations are simplified to the Stokes equations. We employ the three-dimensional Membrane Spectral Boundary Element (MSBE) method [23, 37, 38] to solve interfacial problems in Stokes flows.

2.1 Fluid dynamics

We consider a capsule with viscosity $\lambda\mu$ and density ρ_1 surrounded by an immiscible fluid with viscosity μ and density ρ_2. The capsule's interior and exterior fluids are assumed to be incompressible Newtonian fluids. The characterize size of the capsule is $a = (3V/4\pi)^{1/3}$ where V is the capsule volume. Here, we assume that the membrane permeability is negligible and thus the capsule volume is constant.

An illustration of a basic problem geometry is shown in figure 2.1. The half-height of the constriction channel is ℓ_z. For a rectangular constriction, its half-width is $\ell_y = 2\ell_z$ while its half-length is $\ell_x = \ell_z$. For a square constriction, its half-width

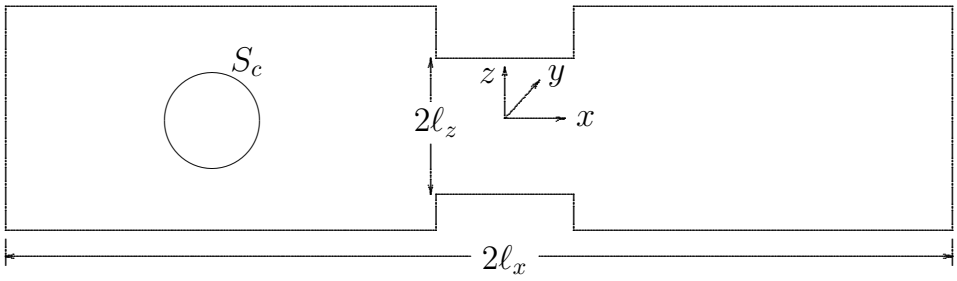

Figure 2.1: Illustration of a capsule in a constriction microchannel.

and half-length are equal to ℓ_z. Both the rectangular and the square constrictions are in the middle of the same outer square microfluidic channel i.e., the half-length and the half-height of the outer square channel are $2\ell_z$ and its half-length is $10\ell_z$.

The undisturbed velocity u_x^∞ in a rectangular channel is given by Yih [79],

$$\frac{u_x^\infty}{\Upsilon} = (\ell_z^2 - z^2) + \sum_{m=1}^{\infty} B_m \cosh\left(\frac{b_m y}{\ell_z}\right) \cos\left(\frac{b_m z}{\ell_z}\right) \tag{2.1}$$

where

$$\Upsilon = -\frac{1}{2\mu}\frac{dp}{dx}, \quad b_m = \frac{(2m-1)\pi}{2}, \qquad B_m = \frac{(-1)^m 4\ell_z^2}{b_m^3 \cosh\left(\frac{b_m \ell_y}{\ell_z}\right)}, \tag{2.2}$$

and p is the dynamic pressure.

After integrating Eq.(2.1), the volumetric flow rate Q over the cross-section area is given by

$$\frac{Q}{\Upsilon} = \frac{8\ell_y \ell_z^3}{3} + \sum_{m=1}^{\infty} B_m \left(\frac{2\ell_z}{b_m}\right)^2 \sinh\left(\frac{b_m \ell_y}{\ell_z}\right) \sin(b_m) \tag{2.3}$$

The average velocity of the exterior fluid far from the capsule is $\mathcal{U} = Q/(\ell_y \ell_z)$ while the maximum undisturbed velocity at the centerline is $\mathcal{U}_{max} \approx 2\mathcal{U}$.

We consider the fluids flow to be in the low-Reynolds-number regime owing to the small size of the capsule and the solid geometry width. Accordingly, the governing equations in the exterior fluid are the Stokes and continuity equations

$$\nabla \cdot \boldsymbol{\sigma} \equiv -\nabla p + \mu \nabla^2 \boldsymbol{u} = 0 \tag{2.4}$$

$$\nabla \cdot \boldsymbol{u} = 0 \tag{2.5}$$

where $\boldsymbol{\sigma}$ is the stress tensor and $\boldsymbol{u}$ the fluid velocity vector. The same equations apply for the interior fluid with the viscosity replaced with $\lambda\mu$.

As shown in figure 2.1, the system surface S_B consists of the capsule interface S_c, the channel surface S_s, and the fluid inlet/outlet surface S_f. At the interface between the capsule and the surrounded fluid, the velocity $\boldsymbol{u}$ is continuous

$$\boldsymbol{u}_1 = \boldsymbol{u}_2 = \boldsymbol{u} \tag{2.6}$$

and the surface stress vector $\Delta \boldsymbol{f}$ is defined by

$$\Delta \boldsymbol{f} \equiv \boldsymbol{n} \cdot (\boldsymbol{\sigma}_2 - \boldsymbol{\sigma}_1), \tag{2.7}$$

where subscripts 1 and 2 denote the capsule's interior and exterior fluids, respectively. Note that $\boldsymbol{n}$ is the unit normal vector pointing to the surrounded fluid. The

boundary conditions are

$$\boldsymbol{u} = 0 \text{ on the solid boundary } S_s, \tag{2.8}$$

$$\boldsymbol{u} = \boldsymbol{u}^\infty \quad \text{or} \quad \boldsymbol{f} = \boldsymbol{f}^\infty \text{ on the fluid surface } S_f \tag{2.9}$$

Here $\boldsymbol{f}^\infty$ is the force associated with the undisturbed channel flow $\boldsymbol{u}^\infty$ on the fluid surface S_f.

The velocity $\boldsymbol{u}$ at any point $\boldsymbol{x}_0$ on the system boundary S_B is determined by a surface integral of the stress vector $\boldsymbol{f} = \boldsymbol{n} \cdot \boldsymbol{\sigma}$ and the velocity $\boldsymbol{u}$ over all points $\boldsymbol{x}$ on the boundary S_B,

$$\begin{aligned} \Omega \boldsymbol{u}(\boldsymbol{x}_0) &= \int_{S_c} [\boldsymbol{S} \cdot \Delta \boldsymbol{f} - \mu(1-\lambda)\boldsymbol{T} \cdot \boldsymbol{u} \cdot \boldsymbol{n}](\boldsymbol{x}) dS \\ &\quad - \int_{S_s} [\boldsymbol{S} \cdot \boldsymbol{f}_2 - \mu \boldsymbol{T} \cdot \boldsymbol{u} \cdot \boldsymbol{n}](\boldsymbol{x}) dS \\ &\quad - \int_{S_f} [\boldsymbol{S} \cdot \boldsymbol{f}_2 - \mu \boldsymbol{T} \cdot \boldsymbol{u} \cdot \boldsymbol{n}](\boldsymbol{x}) dS \end{aligned} \tag{2.10}$$

where Ω takes values $4\pi\mu(1+\lambda)$ and $4\pi\mu$ for points $\boldsymbol{x}_0$ on the capsule interface S_c and the rest boundary, respectively. Here, $\boldsymbol{S}$ represents the fundamental velocity for the three-dimensional Stokes flow and $\boldsymbol{T}$ the corresponding stress,

$$S_{ij} = \frac{\delta_{ij}}{r} + \frac{\hat{x}_i \hat{x}_j}{r^3} \tag{2.11}$$

$$T_{ijk} = -6\frac{\hat{x}_i \hat{x}_j \hat{x}_k}{r^5} \tag{2.12}$$

where $\hat{\boldsymbol{x}} = \boldsymbol{x} - \boldsymbol{x}_0$ and $r = |\hat{\boldsymbol{x}}|$.

The time evolution of the material points of the membrane are determined via the kinematic condition at the interface

$$\frac{d\boldsymbol{x}}{dt} = \boldsymbol{u} \tag{2.13}$$

To produce a closed system of equations, the surface stress $\Delta \boldsymbol{f}$ is determined by the membrane dynamics as discussed in the following section.

2.2 Membrane dynamics

Our membrane description is based on the well-established thin-shell theory and the continuum approach [9, 23, 42, 58] which represent very well capsules and erythrocytes [23, 58] when the typical membrane thickness is much smaller than the size of the capsule/cell. For example, the thickness of alginate capsules or polysiloxane capsules is $O(\mu m)$ to $O(nm)$ where their size is $O(mm)$ [23] while for erythrocytes the membrane thickness is $O(nm)$ and the cell size is $O(\mu m)$.

A membrane shows two basic types of deformation: (i) shearing in-plane with constant surface area, and (ii) extended in-plane with increasing surface area. Each deformation is characterized by a modulus of resistance, i.e., a membrane has a shearing modulus G_s and an area-dilatational modulus G_a.

In the continuum approach, constitutive laws are used to describe the influence of the shearing and the area-dilatation resistance on the membrane tensions τ depending on the material composition of the membrane. These laws represent the relationship between the principal elastic tensions, τ_1^P and τ_2^P, and the principal

stretch ratios, λ_1 and λ_2. The latter are defined as

$$\lambda_\alpha = \frac{ds_\alpha}{dS_\alpha}, \quad \alpha = 1, 2 \text{ (no summation over } \alpha) \tag{2.14}$$

where dS_α and ds_α represent line elements in the reference and deformed shapes, respectively [8].

The Skalak *et al.* law [8, 23, 70] is strain-hardening and thus requires larger tensions than that of a strain-softening membrane law to reach the same extension. The Skalak *et al.* law describes well biological cells (i.e. red blood cells) and membranes obtained by interfacial polymerization,

$$\tau_1^P = \frac{G_s \lambda_1}{\lambda_2}(\lambda_1^2 - 1 + C\lambda_2^2[(\lambda_1\lambda_2)^2 - 1]) \tag{2.15}$$

(τ_2^P is calculated by reversing the λ_β subscripts) where C represents the dimensionless area-dilatation modulus G_a scaled with the shearing modulus G_s.

The hydrostatic traction $\Delta \boldsymbol{f}$ across the membrane, needed in Eq.(2.10), can be written as

$$\Delta \boldsymbol{f} = \Delta \boldsymbol{f}(\text{shearing, area-dilatation}) \tag{2.16}$$

and is determined by $\Delta \boldsymbol{f} = -\nabla_s \cdot \boldsymbol{\tau}$ which in contravariant form gives

$$\Delta \boldsymbol{f} = -(\tau^{\alpha\beta}|_\alpha \boldsymbol{t}_\beta + b_{\alpha\beta}\tau^{\alpha\beta}\boldsymbol{n}) \tag{2.17}$$

where the greek indices range over 1 and 2. In this equation, the $\tau^{\alpha\beta}|_\alpha$ notation

denotes covariant differentiation, $\boldsymbol{t}_\beta$ are the tangent vectors on the capsule surface, and $b_{\alpha\beta}$ is the surface curvature tensor [23, 42, 58].

In addition, we assume that the capsule is (slightly) overinflated and thus prestressed. Such consideration is motivated by the fact that, owing to osmotic effects during their fabrication, artificial capsules are often slightly overinflated as the bioartifucial capsules used in the experimental investigation of Risso, Collé-Pailot, and Zagzoule [63]. To describe the capsule prestress, we define the prestress parameter α_p such that the undeformed capsule (i.e., reference shape) would be scaled by $(1 + \alpha_p)$ [40]. Note that this is mathematically equivalent to scaling the stretch ratios λ_β by $(1 + \alpha_p)$. In our studies, we have used a Skalak capsule with $C = 1$ and $\alpha_p = 0.05$ which implies that the undisturbed capsule is 5% larger than reference shape, i.e., the initial membrane tension is $\tau_0/G_s \approx 0.3401$.

2.3 Definition of problem parameters

To describe the capsule deformation and its transient evolution in the constriction channel, we introduce several geometric and physical properties. To quantify the capsule deformation, we determine the capsule lengths along the three axes, L_x, L_y, and L_z, which are the maximum distances of the capsule surface along the x, y, and z coordinates.

The pressure difference at the channel ends is $\Delta P = P_{in} - P_{out}$ and we also calculate the additional pressure difference owing to the presence of the capsule in

the channel [37],

$$\Delta P^{+} = \Delta P - \Delta P^{0} \tag{2.18}$$

where ΔP is the pressure difference at the channel ends, and ΔP^{0} is the pressure difference at the channel ends when no capsule is present in the channel.

In this research, there are three physical dimensionless parameters which describe the motion of a capsule in a microchannel: the viscosity ratio λ, the scaled area-dilatation modulus C, and the capillary number Ca. The viscosity ratio λ is the ratio of the viscosity of the inner fluid to that of the exterior fluid. The dimensionless parameter C represents the ratio of the area-dilatation modulus G_a to the shearing modulus G_s [8],

$$\frac{G_a}{G_s} = 1 + 2C \tag{2.19}$$

The capillary number Ca is defined as the ratio of viscous flow forces to resistive elastic forces on the membrane,

$$Ca = \frac{\mu \mathcal{U}}{G_s} \tag{2.20}$$

where $\mathcal{U}$ is the average flow velocity in the channel.

2.4 Numerical method

To solve the boundary integral equation (2.10), we employ the three-dimensional Membrane Spectral Boundary Element (MSBE) method [23,37,38]. The system surface is divided into a moderate number of curvilinear quadrilateral elements. The spectral boundary element discretization of the system surfaces includes the channel

surface and the capsule surface as shown in figure 2.2. The geometric and physical variables on each element are discretized using Lagrangian interpolation in term of parametric variables. The basis points (ξ_i, η_j) for the interpolation are chosen the zeros of orthogonal polynomials of Gauss type. This is equivalent to an orthogonal polynomial expansion and yields the spectral convergence associated with such expansions.

The boundary integral equation, Eq.(2.10), consists of two different types of points. The left-hand-side of the equation includes the collocation points $\boldsymbol{x}_0$ where the equation is required to hold while the right-hand-side of the equation contains the basis points $\boldsymbol{x}$ where the physical variables $\boldsymbol{u}$ and $\boldsymbol{f}$ are determined. The MSBE method uses collocation points $\boldsymbol{x}_0$ of Gauss quadrature, i.e., in the interior of the elements. As a result, the boundary integral equation holds even for singular elements, i.e., the elements which contain the corners of the microfluidic channel. In addition, we use basis points $\boldsymbol{x}$ of Gauss-Lobatto quadrature, and thus the physical variables are determined in the interior and on the edges of the spectral elements [23,37,38,77]. For the time integration, we used the 2nd-order Runge-Kutta scheme with a typical time step $\Delta t = 1.0 \times 10^{-4}$.

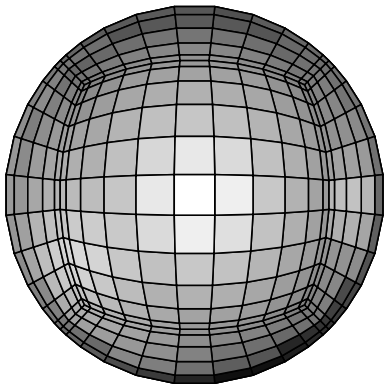

(a)

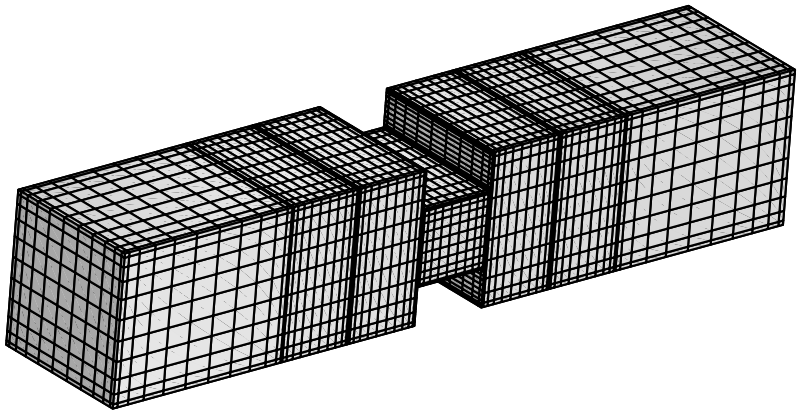

(b)

Figure 2.2: Spectral boundary element discretization of the system surface: (a) the capsule surface, (b) the solid surface of a microfluidic channel along with the fluid surfaces at the channel ends.

Chapter 3: Motion of an elastic capsule in a constricted microchannel

In this chapter, we study the transient dynamics of capsules in a rectangular constriction channel. To our knowledge there are no numerical studies to verify the motion of capsules in a constriction channel. The study of the capsule motion in the constriction has seen an increased interest during the last few decades due to a wide range of applications including drug delivery, cell sorting and cell characterization devices [1, 2, 6, 12, 26, 68], fabrication of microparticles and microcapsules with desirable properties [13, 33, 65], determination of membrane properties [42, 61], and of course its similarity to blood flow in vascular capillaries [55]. For the cell sorting or filtration system in microfluidic devices, the non-cylindrical microchannel are widely used [4, 26, 46].

First, we present the verification of our methodology for capsule motion in a constriction channel by comparing our results with previous experimental results. Next, we investigate the transient dynamics of a capsule and its deformation when the capsule passes through the constriction. We demonstrate the effects of various physical parameters (i.e., capsule size, capillary number and viscosity ratio) on the

capsule motion in the constriction. Furthermore, we compare the motion and deformation of capsule with those of droplets in a constriction owing to see the effects of the membrane enclosed fluid volume.

3.1 Problem description

We consider a spherical Skalak capsule with scaled area-dilatation modulus $C = 1$, moving along the centerline of a constriction microchannel. Three dimensional views of the problem geometry are presented in figure 3.1. The inner fluid of capsule and exterior fluid are Newtonian fluids, with viscosities $\lambda\mu$ and μ, and the same density ρ. The characterize size of the capsule is $a = (3V/4\pi)^{1/3}$ where V is the capsule volume. For the constriction channel, the undisturbed flow far from the capsule is given by equation (2.1).

Assuming low-Reynolds-number flows, Stokes and continuity equations are employed as the governing equations in both fluids. For the system, boundary conditions are shown in detail in chapter 2. The numerical solution of the boundary integral equation is achieved by employing the membrane spectral boundary element method (MSBE) for membranes, which has been described in chapter 2.

The surface discretization of the geometry is illustrated in figure 3.1. For the calculation of capsule in the constriction channel, the computations we performed employ $N_E = 32$ elements. The capsule surface, by being projected onto a cube, is divided into 6 elements as seen in figure 3.1(a). The spectral element discretization of the channel surface follows the capsule's center of mass. The channel surface is

divided into four rows of four elements each as seen in figure 3.1(b). The channel length ℓ_x equal to 10 times the half-size of constriction height ℓ_z. Finally, the channel's inlet and outlet are discretized into one element as shown in 3.1(b). The height of the constriction is $2\ell_z$ and that of the channel is $4\ell_z$. Both the constriction and the channel have width $4\ell_z$. The rectangular constriction has length $2\ell_z$ while the length of the entire microfluidic device is $20\ell_z$. At the beginning of computation, the capsule is located before the constriction at $x_c/\ell_z = -4$. In this work, we used N_B =12-14 basis points i.e., a total number of spectral points for the entire geometry $N = N_E N_B^2$ =4608-6272.

The problem utilized two symmetry planes $y = 0$ and $z = 0$. We use two dimensionless group to describe the capsule flow in a channel: the viscosity ratio λ and the capillary number Ca. Our membrane contains shearing modulus and area-dilatation. The shearing modulus G_s is introduced by the capillary number (i.e., a ratio of viscous flow force to resistive elastic forces on the membrane) such as

$$Ca = \frac{\mu \mathcal{U}}{G_s} \tag{3.1}$$

where $\mathcal{U}$ is the average undisturbed velocity in the channel. The constriction channel's half-height ℓ_z is used as the length scale, the velocity is scaled with the average undisturbed velocity in the constriction $\mathcal{U}$, and the time is scaled with the $\ell_z/\mathcal{U}$. In addition, the pressure is scaled with $\mu\mathcal{U}/\ell_z$, and the membrane tensions with G_s.

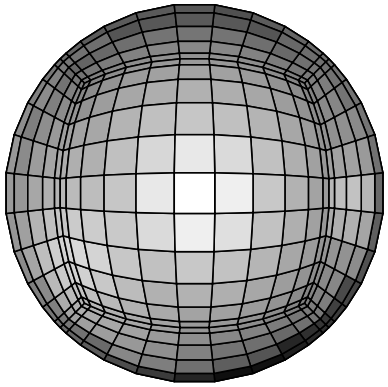

(a)

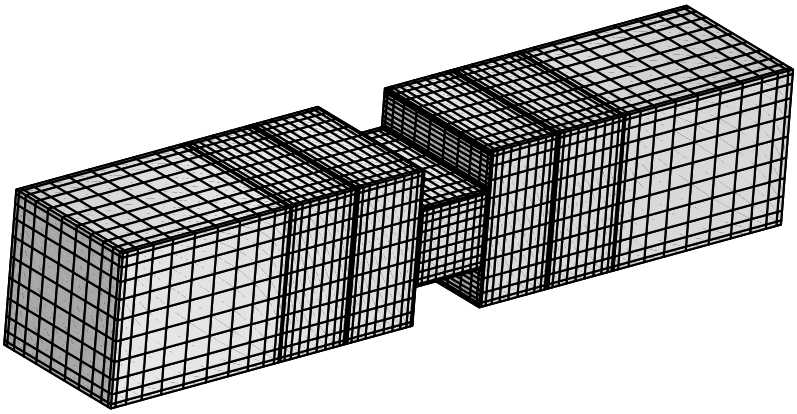

(b)

Figure 3.1: Spectral boundary element discretization of system surface: (a) capsule surface, (b) solid surface of a constriction channel along with the fluid surface at the channel end. Each figure illustrates Lobatto distribution of nodal lines for the corresponding geometry with basis points $N_B = 12$.

Varying parameter	Fixed parameters
$a/\ell_z = 0.2 - 1$	$Ca = 0.1,\ \lambda = 1$
$Ca = 0.01 - 0.1$	$a/\ell_z = 0.7, 1,\ \lambda = 1$
$\lambda = 0.01 - 5$	$a/\ell_z = 0.7, 0.9,\ Ca = 0.1$

Table 3.1: Range of parameters studied in this work. The capsule hardness is $C = 1$ and its prestress $\alpha_p = 0.05$ (or $\tau_0/G_s \approx 0.3401$).

3.2 Validation

In this section, we compare our results with published results for the transient dynamics in the constricted microchannel. To solve our problem, we use our three-dimensional membrane algorithm and calculate the capsule motion along the centerline of a rectangular constricted microchannel. [The spectral boundary element discretization of the channel is seen in Fig. 3.1(b)] The range of dimensionless parameters employed in our computational work (shown in table 3.1) can readily be used in experimental microfluidic systems. As an example, Leclerc *et al.* [42] investigated ovalbumin microcapsules with shear modulus $G_s = 0.07N/m$ in microfluidic channels with a typical height $\ell_z = 50\mu m$. Using as external fluid glycerin with viscosity $\mu \approx 1Pa \cdot s$ and average velocities $\mathcal{U} = 1 - 4\ cm/s$, the authors achieved capillary numbers in the range $Ca \approx 0.1 - 0.5$. Considering erythrocytes with shear modulus $G_s = 2.5\ \mu N/m$ [21, 29] in microfluidic channels with height $\ell_z = O(1)\mu m$ and an external liquid with a viscosity similar to that of water, $\mu \approx 1mPa \cdot s$, the same range of capillary numbers can be achieved with average velocities $\mathcal{U} = O(1)mm/s$.

3.3 Constriction dynamics for equiviscous capsules

In this section we investigate the transient dynamics of a viscous capsule (with viscosity ratio λ=1) as it passes through the microfluidic constriction. We consider a wide range of capsule sizes a, comparable or smaller to the constriction half-length (i.e., a/ℓ_z= 0.2-1) in weak and moderate flow rates Ca. Our results, including the capsule lengths, its velocity U_x and the additional pressure difference ΔP^+ due to the capsule presence, are expressed as functions of the capsule centroid x_c.

The shape of a Skalak capsule as it flows inside the micro-device is shown in figure 3.2. The bullet-like shape of the capsule obtained initially at the left-side of the square channel, e.g. [37], becomes more pointed as the capsule approaches the constriction as shown in figure 3.2(a). This is due to the strong hydrodynamic forces associated with the cross-sectional area decrease which doubles the average fluid velocity inside the constriction since the flow rate Q is fixed in our problem. To balance the deforming hydrodynamic forces, the capsule tries to increase its downstream curvature and decrease its upstream curvature so that the total restoring tension force on the membrane is increased. In essence, this capsule deformation results from the curvature term in the membrane traction, Eq.(2.17), as we identified in our earlier studies on capsule dynamics in planar extensional flows or in microfluidic channels [23, 37, 38].

Thus as the capsule approaches the constriction, its length L_x is increased while its height L_z is decreased considerably, as seen in figure 3.3(a,c). At the same time the capsule width L_y is increased as shown in figure 3.3(b) and thus the

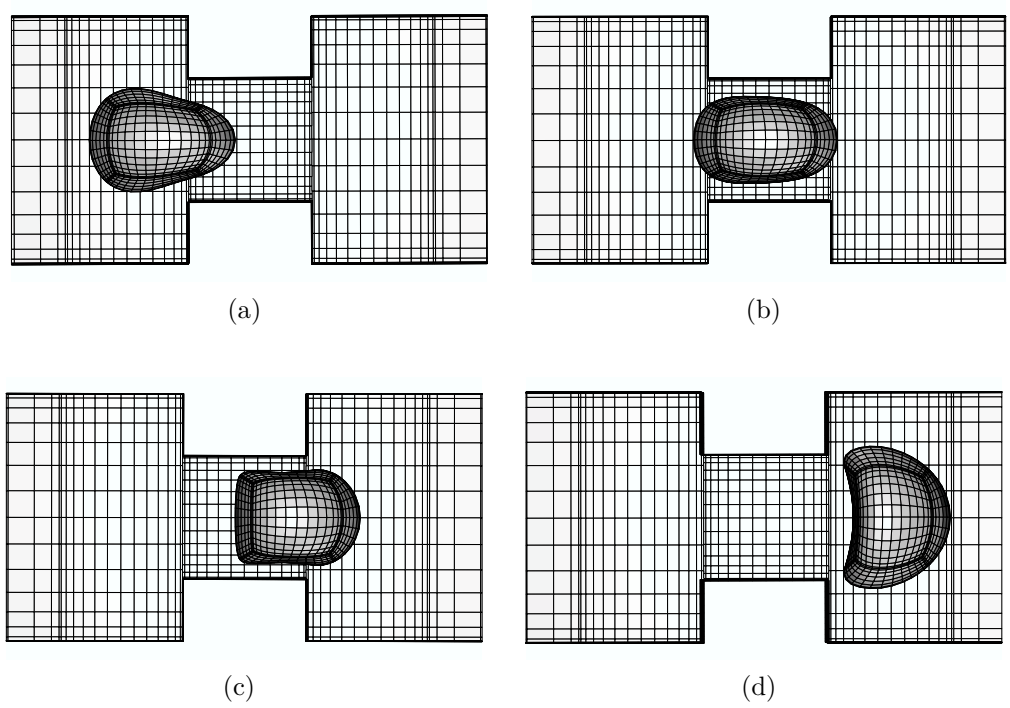

Figure 3.2: The shape of a Skalak capsule with $C = 1$, $a/\ell_z = 1$, $\lambda = 1$ and $Ca = 0.1$ moving inside the microfluidic constriction. The capsules centroid x_c/ℓ_z is (a) -1.51, (b) -0.1, (c) 0.81, and (d) 2.05. The three-dimensional capsule views were derived from the actual spectral grid using orthographic projection in plotting.

capsule tries to occupy a larger area along the less-confined width of the rectangular constriction. This deformation is consistent with the steady-state capsule shape in rectangular channels where the capsule extends significantly in the less-confined lateral direction of the channel cross-section owing to the development of strong lateral tensions on the capsule membrane required for interfacial stability [38].

When the capsule is inside the constriction, i.e., its centroid is nearly $x_c = 0$ as in figure 3.2(b), the capsule has obtained a shape similar to the pebble-like shape characteristic of capsule motion in rectangular channels [38]. This capsule shape involves elongation in the flow and lateral directions, i.e. increased length L_x and L_y, and a significant decrease in its height L_z, as shown in figure 3.3.

As the capsule moves out of the constriction seen in figure 3.2(c), its downstream portion lies at the right-side of the square channel and thus it experiences the dynamics of the cross-section expansion, i.e., the sudden drop of the average fluid velocity. Thus the downstream portion of the capsule slows down; however, its upstream part is still inside the constriction and moves with the faster velocity of the constriction. Both actions result in a compression of the capsule shape and thus in a significant reduction of the capsule length L_x accompanied with a fast increase of its height L_z, as shown in figure 3.3. This expansion effect is much more pronounced as the capsule completely exits the constriction where it obtains a very flattened three-dimensional parachute-like shape, presented in figure 3.2(d), characterized by a higher height L_z compared to its length L_x. (See also the capsule lengths in figure 3.3 when the capsule centroid is nearly $x_c = 2$.) After this peak, the capsule relaxes towards a bullet shape in the square channel far downstream of the constriction.

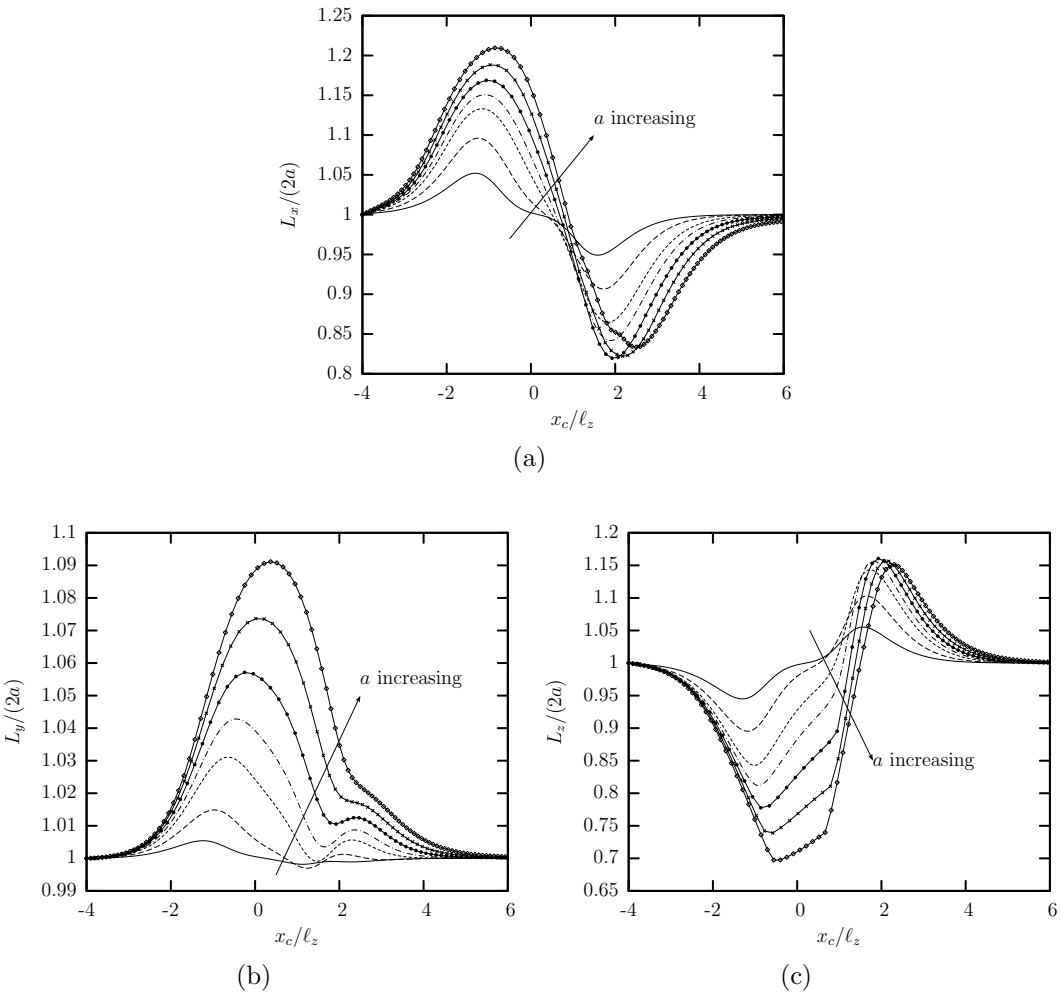

Figure 3.3: Evolution of the capsule lengths as a function of the centroid x_c, for a Skalak capsule with $C = 1$, $Ca = 0.1$ and $\lambda = 1$, for size $a/\ell_z = 0.2, 0.4, 0.6, 0.7, 0.8, 0.9, 1$. (a) Length L_x, (b) width L_y, and (c) height L_z (scaled with the length $2a$ of the undisturbed spherical shape). These lengths are determined as the maximum distance of the interface in the x, y and z directions.

Therefore, the two district regimes associated with the microfluidic constriction, i.e., confinement and expansion, result in two district interfacial shapes. In the confinement regime, the capsule obtains an elongated bullet shape where its length L_x obtains a maximum value and its height L_z a minimum value. The opposite happens during the expansion dynamics where the capsule obtains a flattened parachute shape. Similar deformation has been observed in axisymmetric constrictions where the capsule width is identical to its height (i.e. $L_y = L_z$) due to the axisymmetry [62].

The confinement dynamics are more pronounced as the capsule size a is increased as shown in figure 3.3, since then the capsule occupies a larger volume and thus causes a higher flow blocking. It is of interest to note that due to the rectangular constriction, both the confinement and expansion dynamics are associated with an elongated capsule width L_y, which increases monotonically with the size a, as seen in figure 3.3(b). Therefore, the constriction cross-sectional asymmetry results in a highly non-axisymmetric, fully three-dimensional capsule shape (as shown in figure 3.4), which cannot be described from single-view observations as commonly happens in microfluidic experiments or based on axisymmetric or two-dimensional computations.

In addition, the larger capsule size a (or flow blocking) causes a monotonic decrease of the capsule velocity U_x and an increase of the additional pressure difference ΔP^+ as seen in figure 3.5. Observe that for the equiviscous ($\lambda = 1$) capsules studied in this section, the additional pressure difference ΔP^+ is positive (as also happens for viscous droplets [51]) and thus the capsule presence results in higher

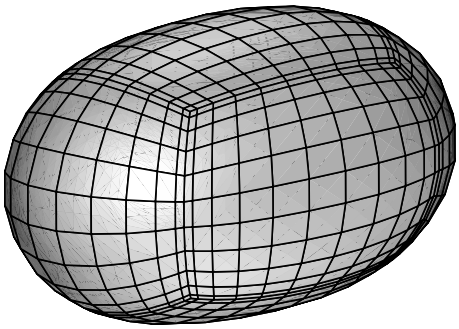

(a)

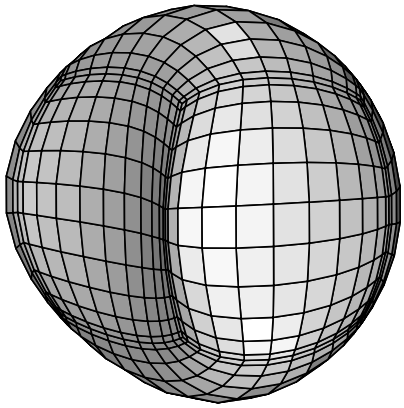

(b)

Figure 3.4: The shape of a Skalak capsule with $C = 1$, $a/\ell_z = 1$, $\lambda = 1$ and $Ca = 0.1$ moving inside the microfluidic constriction for capsules centroid (a) $x_c/\ell_z = -1.51$ and (b) $x_c/\ell_z = 2.05$. The capsule shape is plotted as seen slightly askew from the positive z-axis to reveal its fully three-dimensional conformation.

energy requirements to maintain a constant flow rate.

We emphasize that the effects of decreasing the flow rate Ca (for a given capsule size) are similar to that of increasing the capsule size a (for a given flow rate), since both types of experiments result in a higher flow blocking in the former case due to the reduced interfacial deformation. Thus our results for the flow rate effects for a given capsule size (in particular for $Ca = 0.01 - 0.1$ and a/ℓ_z= 0.7, 0.9) are omitted.

The monotonic variation of the capsule velocity U_x and the additional pressure difference ΔP^+ with the capsule size a or flow rate Ca can be understood by utilizing the scaling behavior we developed for capsule motion in a straight channel [37]. We emphasize that earlier analysis [37] was valid for steady-state capsule motion in straight solid ducts while the current problem involves transient dynamics. However, our computational findings presented in figure 3.5 clearly indicate that the transient dynamics over the entire micro-device scale as the capsule dynamics inside the constriction (e.g. see figure 3.2(c)) which is similar to the dynamics in a straight solid duct. Our conclusion for the current problem is further reinforced by the quasi-steady nature of the Stokes flow.

Therefore, utilizing Eqs.(19) and (27) from Kuriakose and Dimitrakopoulos [37], for capsules with size a comparable to the constriction size ℓ_z, the capsule velocity inside the constriction should scale proportionally with the gap h between the capsule surface and the solid walls,

$$\frac{U_x - \mathcal{U}}{\mathcal{U}} \sim \frac{h}{\ell_z} \tag{3.2}$$

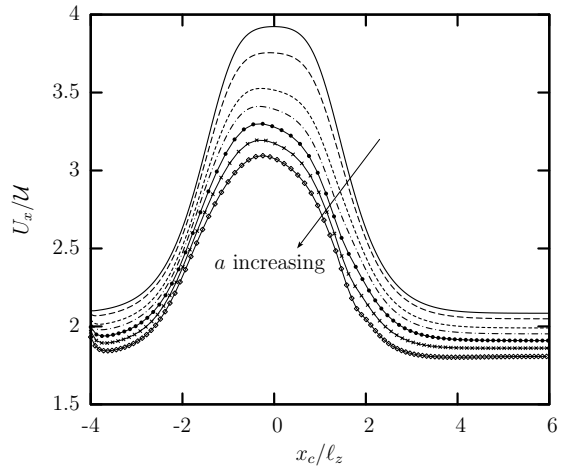

(a)

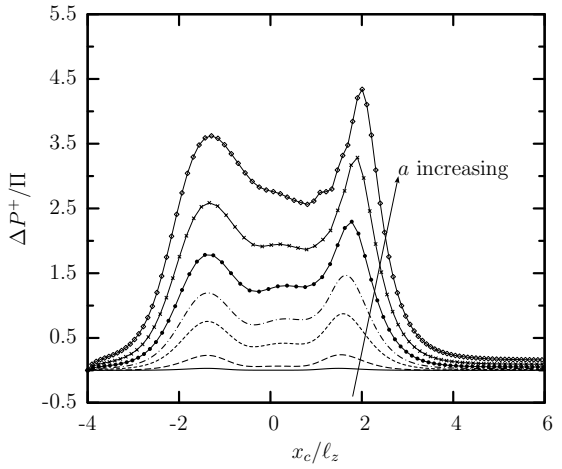

(b)

Figure 3.5: Evolution of (a) the capsule velocity U_x, and (b) the additional pressure difference ΔP^+, as a function of the centroid x_c, for a Skalak capsule with $C = 1$, $Ca = 0.1$ and $\lambda = 1$, for size $a/\ell_z = 0.2, 0.4, 0.6, 0.7, 0.8, 0.9, 1$.

while the additional pressure difference should be inversely proportional to the gap,

$$\frac{\Delta P^+}{\Pi} \sim \frac{\ell_z}{h} \tag{3.3}$$

It is of interest to note that Eqs.(3.2) and (3.3) are formally valid for cylindrical channels, and thus they represent only qualitatively the present problem by considering the gap h between the capsule surface and the solid walls in the xz-plane where the strongest hydrodynamic forces occur owing to the rectangular constriction. As the capsule size a increases (or as the flow rate Ca decreases), the gap h between the capsule surface and the solid walls decreases, and thus the capsule velocity decreases while the additional pressure difference ΔP^+ increases, in agreement with our computational results shown in figure 3.5.

3.4 Effects of viscosity ratio

In this section we investigate the effects of viscosity ratio λ on the transient dynamics of a capsule as it passes through the microfluidic constriction. For this, we consider a capsule with a fixed size $a/\ell_z = 0.9$ and capillary number $Ca = 0.1$, while we vary the viscosity ratio in the range $\lambda = 0.01 - 0.5$, i.e., we investigate from inviscid to very viscous capsules.

Figure 3.6 shows that, for any viscosity ratio, the evolution of the capsule dimensions is similar to that for an equiviscous capsule discussed in section 3.3. In addition, the figure reveals that both in the confinement and the expansion area (i.e., as the capsule enters or exits the constriction), its deformation decreases with the

viscosity ratio. However, during the final relaxation stage towards the bullet shape in the square channel far downstream from the constriction, it is the very viscous capsule with $\lambda = 5$ which is more deformed since capsules with smaller viscosity ratio relax faster.

To explain the effects of the viscosity ratio on the capsule deformation, we need to consider that the capsule is deformed owing to the combined effects of the surrounding and inner fluids normal stresses on the capsule interface. Therefore, the capsule transient dynamics is characterized by the membrane time scale necessary to reach steady state, which for a given membrane hardness C is given by

$$\tau_m \sim (1 + \lambda) Ca \frac{a}{\ell_z} \tau_f \tag{3.4}$$

where $\tau_f = \ell_z / \mathcal{U}$ is the flow time scale. (More details on this time scale are given in Park and Dimitrakopoulos [53].) For low enough viscosity ratio, e.g. for $\lambda \leq 0.01$ in our problem, the inner fluid does not practically participate in the transient dynamics, and thus all low-viscosity capsules show identical evolution, in agreement with our computational results shown in figure 3.6. For moderate viscosity ratios, $\lambda = O(1)$, both the inner and the surrounding fluids affect the capsule deformation, while for very viscous capsules (e.g. $\lambda = 5$), it is the inner fluid which mostly affects the capsule deformation.

As the viscosity ratio λ increases, the time necessary for the capsule to react to the flow changes imposed by the constriction (i.e., the time scale τ_m) is increased. This makes the deformation rate slower and thus the capsules transient deformation

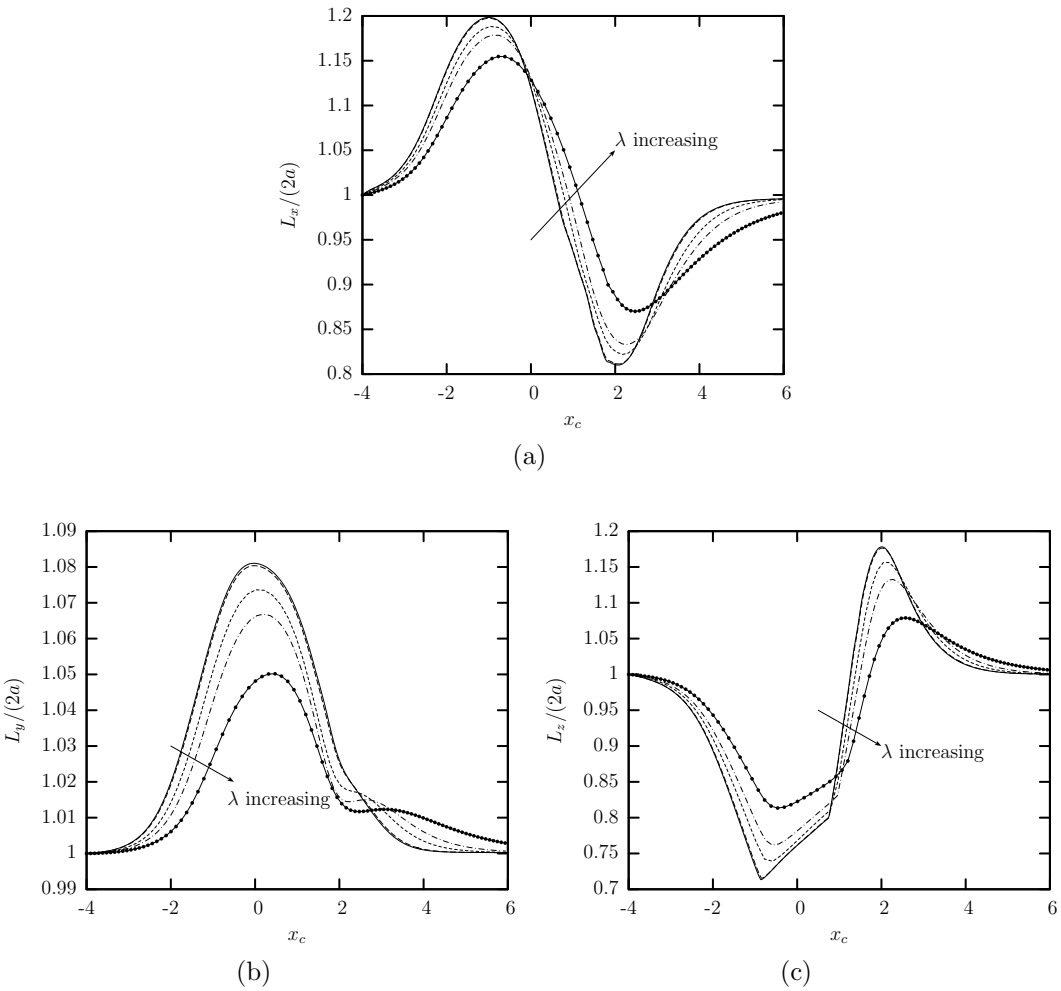

Figure 3.6: Evolution of the capsule lengths as a function of the centroid x_c, for a Skalak capsule with $C = 1$, $a/\ell_z = 0.9$ and $Ca = 0.1$, for viscosity ratio $\lambda = 0.01, 0.1, 1, 2, 5$. (a) Length L_x, (b) width L_y, and (c) height L_z (scaled with the length $2a$ of the undisturbed spherical shape). Our results for $\lambda = 0.01$ are identical for lower viscosity ratios, e.g. $\lambda = 0.001, 0$, and thus represent the low-viscosity limit $\lambda \ll 1$.

decreases with the viscosity ratio as seen in figure 3.6. For the same reason, during the final relaxation stage towards the bullet shape far downstream from the constriction, the very viscous capsule with $\lambda = 5$ needs a significant time (or channel length) to reach equilibrium while the capsules with smaller viscosity ratio relax faster, in agreement with Eq.(3.4) and our computational findings shown in figure 3.6.

In contrast to the viscosity effects on the capsule deformation, the capsule velocity U_x is practically not affected by λ, and thus all capsules show the same increase in U_x as they pass through the constriction, as seen in figure 3.7(a). Similarly, the viscosity ratio has very weak effects on the additional pressure difference ΔP^+ which is positive for all viscosity ratios (even for inviscid capsules with $\lambda \ll 1$), as shown in figure 3.7(b).

3.4.1 Comparison with droplet dynamics

Owing to the rather unexpected behavior of the capsule velocity U_x and the additional pressure difference ΔP^+ not to be affected much by the viscosity ratio, we proceed now by investigating the corresponding effects on the droplet deformation. A droplet is also a deformable object but, in contrast to a capsule, its surface tension γ remains constant. Thus, our goal here is to clarify the similarities and differences of droplet and capsule transient dynamics as they pass through the microfluidic constriction. To determine the droplet dynamics, we utilized our fully-implicit time-integration spectral algorithm for droplets [20] as well as our mem-

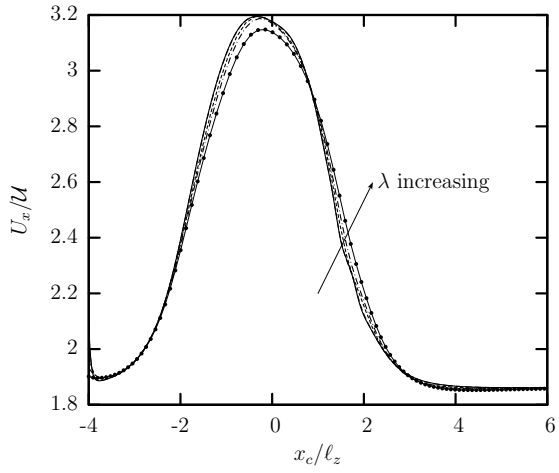

(a)

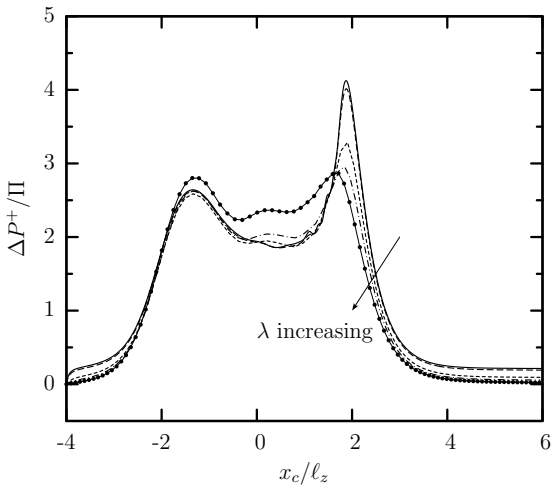

(b)

Figure 3.7: Evolution of (a) the capsule velocity U_x, and (b) the additional pressure difference ΔP^+, as a function of the centroid x_c, for a Skalak capsule with $C = 1$, $a/\ell_z = 0.9$ and $Ca = 0.1$, for size $\lambda = 0.01, 0.1, 1, 2, 5$.

brane spectral boundary element algorithm by imposing surface-tension interfacial conditions, which is identical to our explicit time-integration spectral algorithm for droplets [76]. In this case, the capillary number is defined as $Ca = \mu\mathcal{U}/\gamma$ where γ is the droplets surface tension.

A comparison of the deformation of droplets and capsules, as in figures 3.8 and 3.6, reveals that the droplets length L_x and height L_z deform similarly to those for a capsule, as both soft particles pass through the microfluidic constriction. It is of interest to note that similar interfacial deformation was also found, both computationally and experimentally, for nearly-spherical vesicles in microchannels with oscillating height [10, 50]. In essence, the deformation of the particles length and height is a pure hydrodynamic effect due to the significant changes in the flow caused by the constriction.

On the other hand, the droplets lateral dimension (i.e., its width L_y) shows a smaller deformation than that for a capsule. Furthermore, the width L_y of the droplet increases only during the confinement area where the droplet enters the constriction, and decreases during the expansion area where the droplet exits the constriction, while the capsule remains laterally elongated over the entire constriction. The different evolution of the width of the two soft particles in the rectangular constriction is similar to the difference in the steady-state shapes of droplets and capsules in rectangular channels identified in our recent work [38]. In particular, in asymmetric channel flows, a capsule extends significantly along the less-confined lateral direction of the channel cross-section (i.e., the channel width) to facilitate the development of strong lateral tensions required for interfacial stability. Such

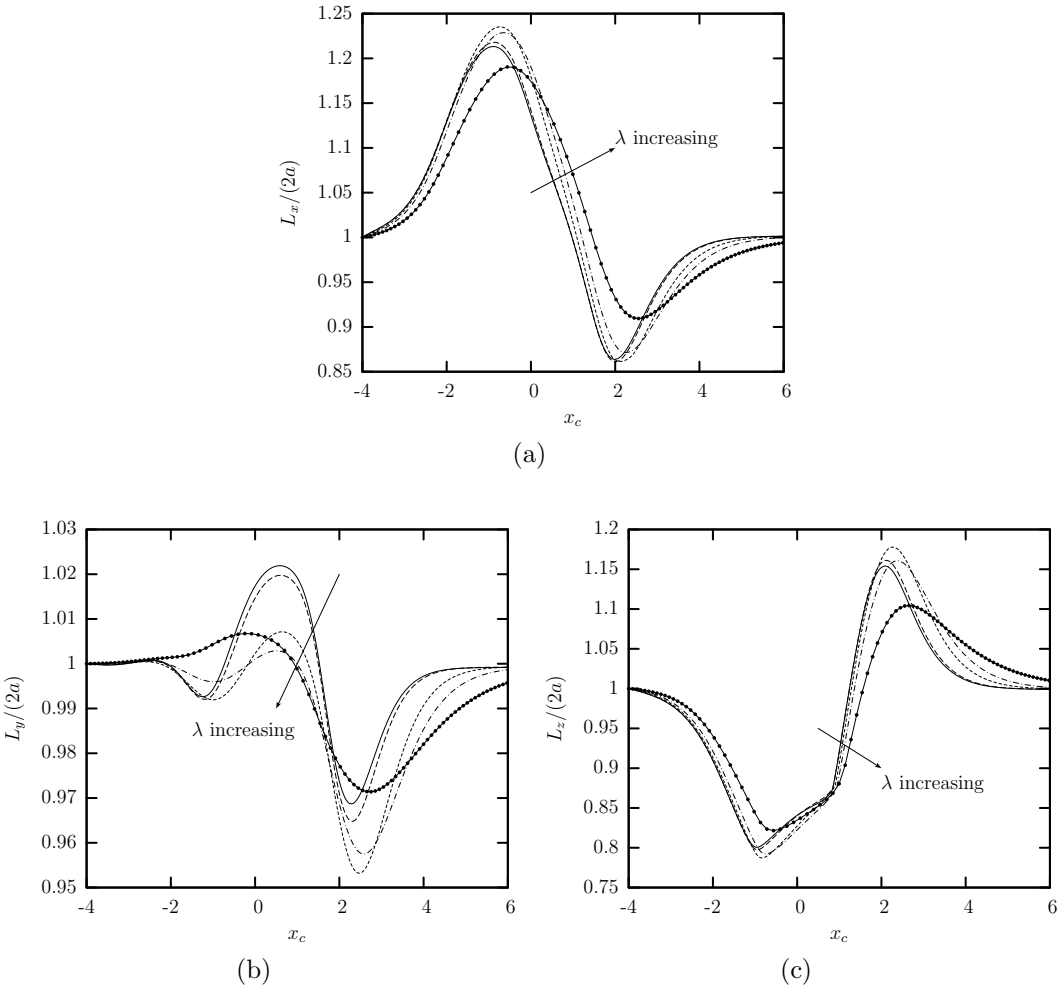

Figure 3.8: Evolution of the droplet lengths as a function of the centroid x_c, for a droplet with $a/\ell_z = 0.9$, $Ca = 0.1$ and viscosity ratio $\lambda = 0.01, 0.1, 1, 2, 5$. (a) Length L_x, (b) width L_y, and (c) height L_z (scaled with the length $2a$ of the undisturbed spherical shape). Our results for $\lambda = 0.01$ are identical for lower viscosity ratios, e.g. $\lambda = 0.001, 0$, and thus represent the low-viscosity limit $\lambda \ll 1$.

deformation is not required for a droplet owing to its a constant surface tension, and thus in the present problem, the droplet width, after the initial increase in the confinement area, reduces in the expansion area to facilitate the flattened parachute shape as the droplet exits the constriction.

The major differences in the motion of the two soft particles involve the velocity U_x and the additional pressure difference ΔP^+, which in the case of a droplet are affected significantly by the viscosity ratio λ as shown in figure 3.9. In contrast to the practically insensitive capsules, the velocity of a droplet decreases with the viscosity ratio. The same is true for its additional pressure difference ΔP^+ which for a droplet is negative for low enough viscosity ratios. It is of interest to note that the evolution of the velocity U_x and the additional pressure difference ΔP^+ for a very viscous droplet (e.g. $\lambda = 5$) is very similar to that for the capsule (at any viscosity ratio). Therefore, even under the transient conditions imposed by the microfluidic constriction, capsules with any viscosity ratio correspond better to very viscous droplets, as we identified for steady-state capsule motion in solid ducts [37].

3.4.2 Reasoning for the transient dynamics of droplets and capsules

To explain the different effects of the viscosity ratio on the transient velocity U_x and the additional pressure difference ΔP^+ of droplets and capsules over the constriction, we need to to consider the fluid circulation inside the soft particles.

For the case of droplets, where the interface is just a separation of two fluid

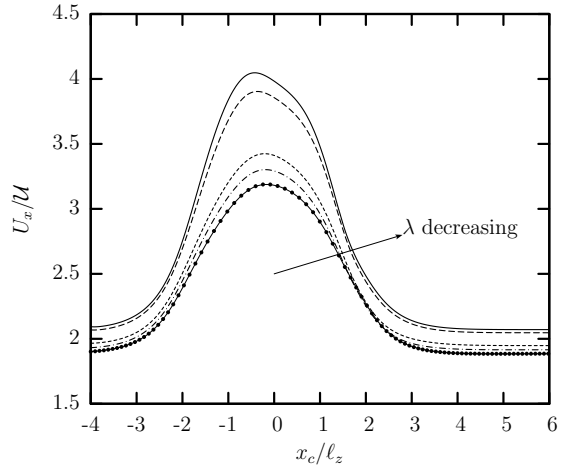

(a)

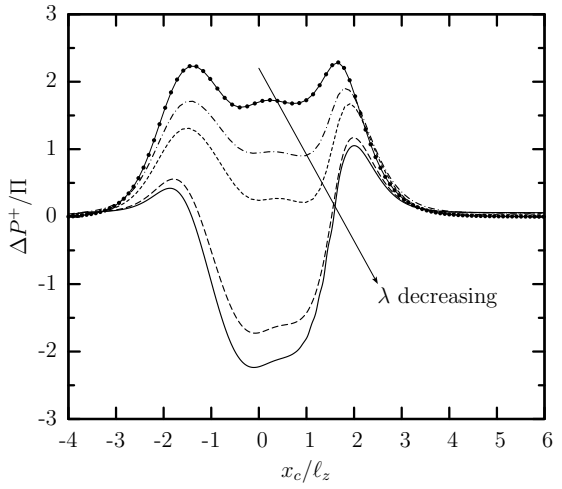

(b)

Figure 3.9: Evolution of (a) the capsule velocity U_x, and (b) the additional pressure difference ΔP^+, as a function of the centroid x_c, for a Skalak capsule with $C = 1$, $a/\ell_z = 0.9$ and $Ca = 0.1$, for size $\lambda = 0.01, 0.1, 1, 2, 5$.

phases with no material, there may be a significant inner circulation (with respect to the translation motion) owing to the continuity of the interfacial shear stresses from the surrounding and inner fluids. Thus, complex streamline patterns have been found for steady-state droplet motion in solid ducts; for example, see figure 3 from Ho and Leal [30] and figure 3(a) from Lac and Sherwood [41]. The same is true for unsteady droplet motion such as its passing through the microfluidic constriction studied in this work. For low-viscosity ratio, the inner circulation is as significant as the droplet translation velocity U_x. This is shown for $\lambda \leq 0.1$ in table 3.2, where we calculated the maximum and average of the absolute value of the interfacial shear velocity (with respect to the droplet translation velocity U_x) as the capsule passes through the constriction. Note that the magnitude of the interfacial shear velocity represents very well the strength of the inner circulation. As the viscosity ratio increases, the inner circulation becomes weaker, e.g. its representative velocity is reduced compared to the droplet translation velocity U_x, as seen in table 3.2 for $\lambda = 1, 2$. For very viscous droplets, the inner circulation becomes negligible (as shown in table 3.2 for $\lambda = 5$), and eventually for $\lambda \to \infty$ the droplet solidifies, the inner circulation becomes zero and the entire droplet moves with its translation velocity U_x only.

For the case of capsule motion in solid ducts, at steady state there is no flow inside the capsule owing to the specific symmetry of the channel flow and the material interface, i.e., the elastic-solid membrane [37, 58]. Thus, the steady-state capsule motion in duct flows corresponds better to the dynamics of high-viscosity ($\lambda \gg 1$) droplets since at steady state both soft particles translate in the duct flow

Table 3.2: Maximum and average of the absolute value of the shear velocity on the surface of a droplet or capsule (in the reference frame moving with the soft particle), when the particle is in the middle of the constriction (i.e., $x_c \approx 0$), for $a/\ell_z = 0.9$, $Ca = 0.1$ and several viscosity ratios λ. Also included is the particle velocity U_x for comparison reasons. (The velocity scale is the average undisturbed velocity $\mathcal{U}$ in the square channel.) Similar results we obtain when the capsule enters or exits the constriction.

Material	λ	$U_{x,c}$	$\lvert U_x\rvert_{max.}$	$\lvert U_y\rvert_{max.}$	$\lvert U_z\rvert_{max.}$
Capsule	0.01	3.1752	0.1970	0.1602	0.2628
	0.1	3.1751	0.1920	0.1568	0.2536
	1	3.1679	0.1521	0.1235	0.2017
	2	3.1652	0.1408	0.1003	0.1607
	5	3.1380	0.1028	0.0680	0.1009
Drop	0.01	3.9680	3.2646	0.4768	0.9439
	0.1	3.8529	2.9522	0.4082	0.8605
	1	3.4111	1.6207	0.1773	0.4542
	2	3.2916	1.1299	0.1947	0.3014
	5	3.1819	0.6601	0.1560	0.1775

Material	λ	$U_{x,c}$	$\lvert U_x\rvert_{avg.}$	$\lvert U_y\rvert_{avg.}$	$\lvert U_z\rvert_{avg.}$
Capsule	0.01	3.1752	0.1083	0.0341	0.0842
	0.1	3.1751	0.1068	0.0330	0.0821
	1	3.1679	0.0936	0.0275	0.0706
	2	3.1652	0.0836	0.0222	0.0598
	5	3.1380	0.0608	0.0159	0.0419
Drop	0.01	3.9680	1.3357	0.2941	0.3365
	0.1	3.8529	1.1618	0.2377	0.3021
	1	3.4111	0.5161	0.0700	0.1509
	2	3.2916	0.3446	0.0466	0.1021
	5	3.1819	0.1853	0.0289	0.0595

as solids with zero inner velocity, as discussed in our earlier papers [37, 38].

During transient, non-tank-treading capsule motion, as in the current problem, the deformation of the capsule should create some inner circulation. To determine how significant this inner motion is, in table 3.2 we also include information on the magnitude of the interfacial shear velocity (with respect to the translation velocity U_x) for capsules inside the constriction with several viscosity ratios. In contrast to droplets, the circulation inside a capsule passing through the constriction remains always small (compared to its translation velocity U_x), even at low viscosity ratios.

Therefore, owing to restrictions imposed by the material membrane, the transient, non-tank-treading capsule deformation is always accompanied with a weak inner circulation, and thus the viscosity ratio does not affect much the capsule velocity U_x and the additional pressure difference ΔP^+, as shown earlier in figure 3.7. In addition, the weak inner circulation results in a positive additional pressure difference ΔP^+ even for low-viscosity capsules with ($\lambda \ll 1$), in direct contrast to low-viscosity droplets which create a negative ΔP^+. In essence, owing to the weak inner circulation, during transient, non-tanktreading motion, capsules at any viscosity ratio still correspond to high-viscosity ($\lambda \gg 1$) droplets, as at steady state [37, 38].

It is of interest to note that low-viscosity capsules are more deformed than very viscous capsules as discussed earlier around Eq.(3.4), and thus they show a more flattened parachute shape as they exit the constriction, characterized by a higher height L_z as seen in figure 3.6(c) for $x_c/\ell_z \approx 2$. The larger flow blocking of the more deformed shapes causes a higher peak in the positive additional pressure

difference ΔP^+ of low-viscosity capsules in the expansion area, shown in figure 3.9(c) for $x_c/\ell_z \approx 2$.

Chapter 4: Hydrodynamic forces exerted on a microfluidic constriction owing to a capsule passing

4.1 Introduction

In this chapter, we investigate the hydrodynamic forces exerted on the constriction owing to a capsule passing through the microgeometry as described in chapter 3. The study of hydrodynamic forces has seen an increased interest owing to its important role in cell segregation [3, 75], filtration systems [36, 46, 80, 81] and biomedical fields [2, 28, 32, 77, 78].

In microfluidics, the understanding of hydrodynamic forces is very important for designing filtration systems, cell sorting or the pattering on the microdevices. Zhu *et al.* [81] calculated the capsule deformation and the fluid velocity when the capsule passed the rigid constricted microchannel. Their results showed that the adhesive strength between the capsule and the constriction and the capsule's stiffness strongly affect the capsule dynamics. Furthermore, Zhu *et al.* [80] investigated the capsule dynamics as it passed through deformable constrictions. They calculated

the energy associated with the adhesion between the capsule and the constriction. Alexeev *et al.* [2] studied the selectively entrapped or bursting microcapsules on a substrate with varying adhesive strength. The capsule stiffness and the adhesive interaction on the substrate are major factors for the capsule bursting and its velocity. Furthermore, they measured the energy associated with the adhesive interaction between the rolling capsule and a substrate and the capsule deformation [3]. Pozrikidis [60] investigate the force and torque exerted on a spherical particle when the particle straddles a flat interface in a simple shear flow. The author studied the particle translational and angular velocities for any viscosity ratio. Mao and Alexeev [46] computed the stream velocity distribution in diagonal protuberances from the opposite channel walls as microparticles passing for varying Reynolds number.

In biomedical fields, the hydrodynamic force is a key factor to understand the physiological inflammation response in the microcirculation such as leukocytes migration, rolling and adhesion to the vascular endothelium cells. Leukocyte migration, rolling, adhesion and detachment are essential steps in the immune response system to inflammation. The inflammation process begins with the migration of leukocytes in the postcapillary venules [27, 47]. Once a leukocyte contact in the endothelial cells, the leukocyte can interact with endothelial cells via receptor-ligand binding. If the binding force is weak, the leukocyte may begin to roll along the endothelial cells [5, 15]. When the binding force becomes strong, the leukocyte is attached to the endothelial cells [24]. For the adhesion of leukocytes on the endothelial cells, leukocytes should be under the force balance between the receptor-ligand binding forces on the surface and the hydrodynamic forces by the blood flow [57, 77].

Several studies have focused on the fluid forces on protuberances such as adhering cells on the vessel surface or the flow sediments by flow on the microchannel. Pozrikidis [56] computed the hydrodynamic force, torque exerted on hemisphere-shaped protuberances and stream-lines over the protuberances in a simple shear flow. Furthermore, Pozrikidis [57] extended his research by considering the effect of a pressure gradient on axisymmetric shapes of protuberances, i.e., hemisphere and rectangular shapes. The drag force and torque are computed over the protuberances in a parabolic flow. Gaver and Kute [28] studied the fluid stresses on a cell adhering to a microchannel wall. They considered a two-dimensional flow within two parallel plates and a semicircular bump. They investigated the effects of adherent cell sizes on the fluid forces. Dong *et al.* [24] numerically investigated the mechanics of leukocyte deformation and adhesion to endothelial cells in shear flow. They studied the drag force and torque for the leukocyte deformation, adhesion to endothelial cells and disruption of adhesive bonds with varying the mean-blood velocity. Sugihara-Seki and Schmid-Schönbein [72] determined the shear stress distribution on the leukocyte and its vicinity for adherent, rolling, and free-suspended leukocytes. Wang and Dimitrakopoulos [77, 78] investigated the effects of the components of the hemodynamic force i.e., the shear and normal forces, on an adhering endothelial cell, leukocyte and their vicinity. They investigated varying sizes of blood vessels and cell's spreading angles. Furthermore, they developed a scaling analysis for the shear and normal forces exerted on the adherent cell. Couzon *et al.* [18] experimentally verified the critical stresses for cell detachment from the microchannel walls. They focused on the characteristics of shear stress as a function of the number of adhesion

sites, bonding force and the microchannel size. Khismatullin and Truskey [35] investigated the effect of cytoplasmic viscosity on the the hydrodynamic force, bonding force and lift force on a rolling P-selectin-mediated leukocyte as a function of time.

In the studies mentions above, the exterior fluid was modeled as a Newtonian fluid and they considered a single protuberance or adhering leukocyte. Das *et al.* [19] investigated the effects of leukocyte adhesion for the non-Newtonian Casson fluid flow in small venules. They considered the effects, on the resistance and shear stress, of the position of adhered leukocytes inside the blood vessel. Pappu *et al.* [52] investigated the flow resistance and the fluid drag force over an adhesive rolling of deformable leukocytes by using a three-dimensional computational modeling and the immersed boundary method. Based on their results, the flow resistance and the drag force over the adherent leukocytes are strongly affected by the ratio of the fluid center velocity to the half channel height, number of adherent leukocytes and cell concentration. Pickard and Ley [54] experimentally observed velocity profiles over adherent leukocytes on the microvessel by using microparticle tracking velocimetry and determined the shear stress on adherent leukocytes. They also measured adhesive force and the peeling tension acting on the vicinity of adherent leukocytes. Sequeiraa *et al.* [66] computed the flow velocity, wall shear stress and torques around an adherent spherical leukocyte on the endothelial wall of a cylindrical venule by considering an incompressible shear-thinning blood flow model. Christ *et al.* [14] experimentally studied the cell adhesion strength as a function of the number of cells and the cell's contact area on the wall. Their simulation results showed that the distribution of shear stress over an adherent cell depends on the height and the

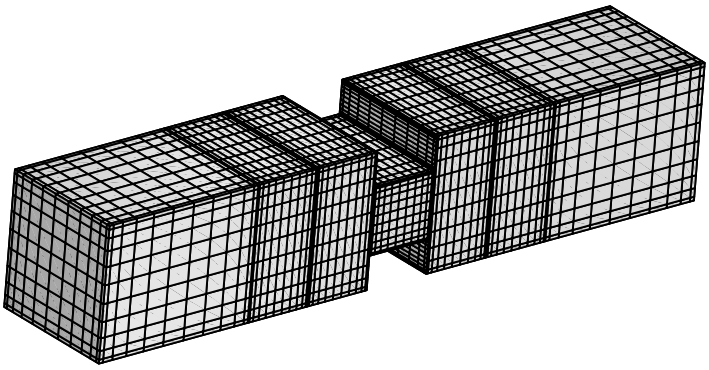

Figure 4.1: Illustration of the constricted microchannel.

contact area of cells at a fixed cell volume on the wall.

Few studies have considered the cell flow over the protuberances or adherent leuckocytes. Freund [27] numerically investigated the flow mechanics around a leukocyte when red blood cells flow over the leukocyte. The author verified that the fluid flow over the leuckocyte is strongly affected by the stiffness of red blood cells and mean blood flow velocity. Isfahani and Freund [32] studied the forces on the wall-adhered leukocyte as the red blood cells pass by corresponding homogeneous blood models. They focused on the effects on the leukocyte geometry and hematocrit on the forces exerted on the adherent leukocyte in a microvessel.

In our work, we focus on the hydrodynamic force and its components, i.e., the shear and normal forces, exerted on the rectangular constriction in a square microchannel duct owing to a capsule passing described as shown in figure 4.1. First, we study the effects of flow rate Ca, capsule size a, and viscosity ratio λ on the hydrodynamic force and its components over the rectangular constriction. Second, we compare the effects of the passing capsule or droplet flow on the hydrodynamic

forces over the rectangular constriction.

4.2 Definition of physical variables

In our work, we consider the exterior and interior fluids to be Newtonian fluids at a low-Reynolds-number flows. The capsule used in our work has a spherical quiescent shape. We investigate the hydrodynamic force and its components (i.e., shear and normal forces) over the rectangular constriction as the soft particle moves inside the microfluidic channel shown in figure 4.1.

The hydrodynamic force F_x exerted on the rectangular constriction is given by

$$F_x = \int_{S_{const}} f_x dS \tag{4.1}$$

where S_{const} is the constriction surface area and f_x the force along x-axis on the constriction. The shear force F_x^{sh} and the normal force F_x^n exerted on the rectangular constriction are given by

$$F_x^{sh} = \int_{S_{const}} f_x^{sh} dS \quad \text{and} \quad F_x^n = \int_{S_{const}} f_x^n dS \tag{4.2}$$

where f_x^{sh} is the x-component of the shear stress, i.e., $f_x^{sh} = (\sqrt{(f_x^L)^2 + (f_y^L)^2})_x$, f_x^n is the x-component of the normal force, $f_x^n = (f_z^L)_x$, on the constriction and S_{const} is the constriction's surface area. We note that $\boldsymbol{f}^L = (f_x^L, f_y^L, f_z^L)$ is the force vector defined at the local Cartesian coordinate system (x^L, y^L, z^L) where x^L and y^L axes are on the tangent plane at each surface point and the z^L axis is parallel to the

normal vector $\boldsymbol{n}$.

We calculate the additional hydrodynamics force F_x^+, the additional shear force F_x^{sh+} and additional normal force F_x^{n+} exerted on the constriction owing to the capsule passing. The additional hydrodynamic force F_x^+ is given by

$$F_x^+ = F_x - F_x^0 \tag{4.3}$$

where F_x^0 is the hydrodynamic force exerted on the constriction in the absence of the capsule in the microchannel. The additional shear and additional normal forces are defined by

$$F_x^{sh+} = F_x^{sh} - F_x^{sh,0} \quad \text{and} \quad F_x^{n+} = F_x^n - F_x^{n,0} \tag{4.4}$$

where $F_x^{sh,0}$ is the shear force and $F_x^{n,0}$ the normal force exerted on the constriction when no capsule is present in the microchannel.

As mentioned in chapter 2, the height of the constriction is $2\ell_z$. The constriction half-height ℓ_z serves as the length scale for the present problem. In this work, the constriction surface area is $S_{const} = 32\ell_z^2$ and ℓ_z^2 serves as the scale of the constriction surface area. The average undisturbed velocity $\mathcal{U}$ in the square channel is used as the velocity scale. The shear stress τ on the constriction is scaled with the undisturbed shear stress on the solid wall $\tau_{wall}^{\infty} = \mu\mathcal{U}/\ell_z$. Based on Eq.(4.1), $F_x \sim \ell_z^2 f_x \sim \ell_z^2 \tau_{wall}^{\infty}$ and thus we employ $\ell_z^2 \tau_{wall}^{\infty}$ as the scale for the hydrodynamic force exerted on the constriction due to the capsule passing.

4.3 Effects of flow rate and capsule size

We investigate now the effects of the capsule size a and flow rate Ca on the hydrodynamic forces exerted on the constriction channel owing to the capsule passing.

Figure 4.2 shows the effects of flow rate Ca and capsule size a on the hydrodynamic force exerted on the constriction and the additional hydrodynamic force. Both F_x and F_x^+ decrease with increasing flow rate Ca, while both forces increase with increasing capsule size a. The increase of the hydrodynamic force F_x and the additional hydrodynamic force F_x^+ is much more pronounced at lower flow rates and larger capsule sizes owing to a higher flow blocking.

The larger capsule size a (or the lower flow rate Ca) causes an increase of the shear force F_x^{sh} and the additional shear force F_x^{sh+} as seen in figure 4.3 and 4.4. The normal force F_x^n and the additional normal force F_x^{n+} are increased with increasing of capsule size a (or decreasing flow rate Ca) as shown in figure 4.3 and 4.4. The additional shear F_x^{sh+} and normal F_x^{n+} forces are positive for $\lambda = 1$.

To explain this, we utilize the scaling analysis of Wang and Dimitrakopoulos [77], i.e., the shear force F_x^{sh} is proportional to the shear stress τ_{const} and the constriction surface area S_{const},

$$F_x^{sh} \sim \tau_{const} S_{const} \tag{4.5}$$

while the normal force F_x^n is proportional to the pressure difference ΔP^{const} over

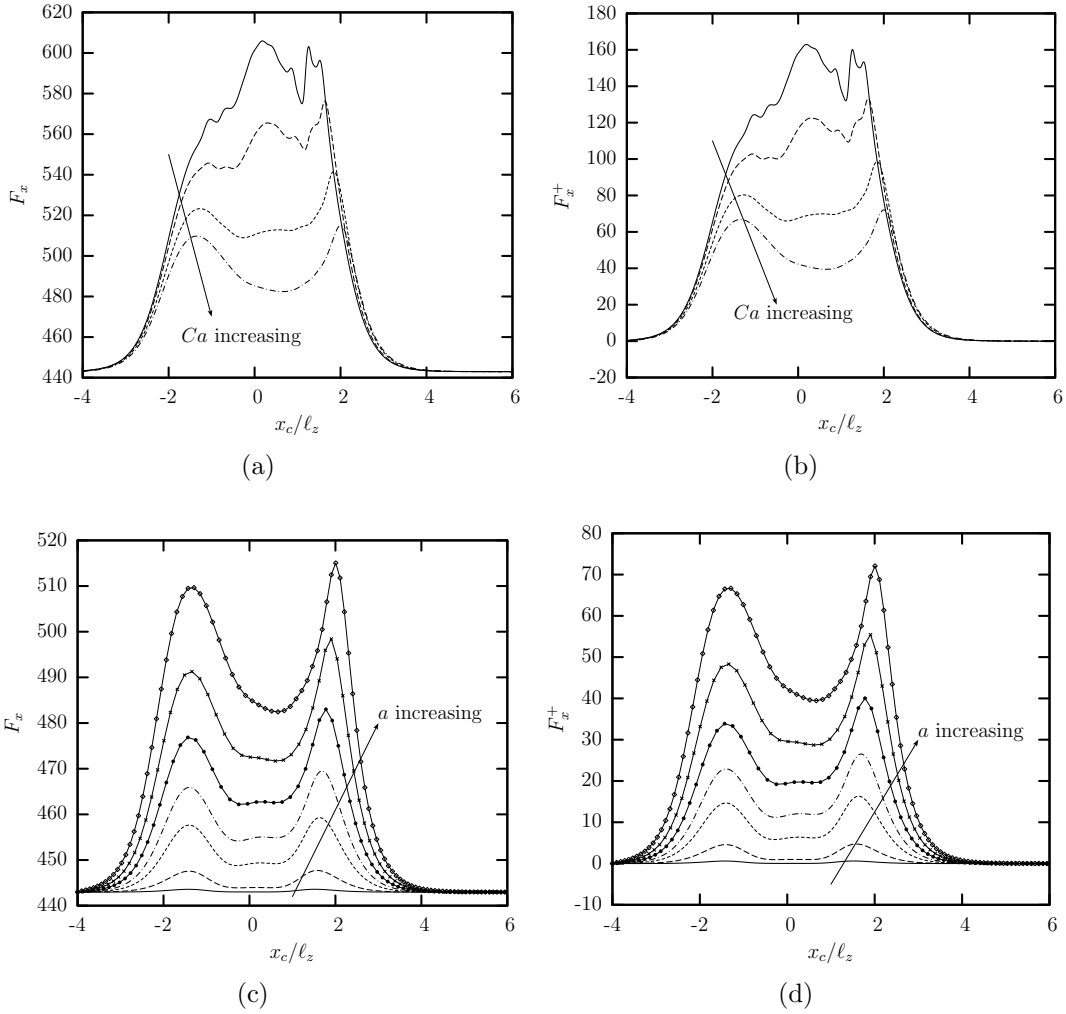

Figure 4.2: The hydrodynamic forces on the constriction as a function of the capsule centroid x_c, for a Skalak capsule with $C = 1$ and $\lambda = 1$. Effects of the flow rate $Ca = 0.01, 0.02, 0.05, 0.1$ for capsule size $a/\ell_z = 1$ on (a) the hydrodynamic force F_x and (b) the additional hydrodynamic force F_x^+ exerted on the constriction. Effects of the capsule size $a/\ell_z = 0.2, 0.4, 0.6, 0.7, 0.8, 0.9, 1$ for flow rate $Ca = 0.1$ on (c) the hydrodynamic force F_x and (d) the additional hydrodynamic force F_x^+ exerted on the constriction.

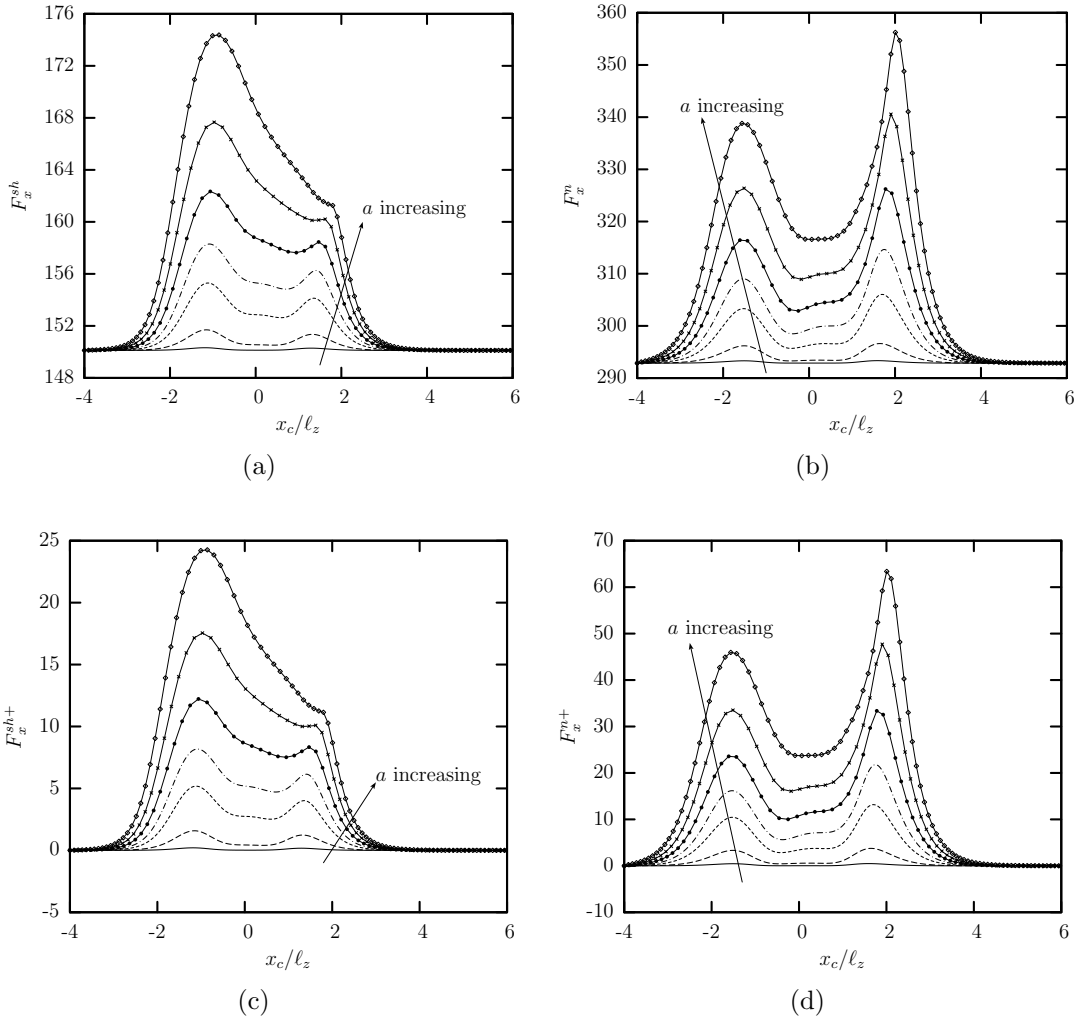

Figure 4.3: Effects of the capsule size a/ℓ_z on the shear and normal forces on the constriction for a Skalak capsule with $C = 1$, $\lambda = 1$ and $Ca = 0.1$. (a) Shear force F_x^{sh}, (b) normal force F_x^{n}, (c) additional shear force F_x^{sh+}, and (d) additional normal force F_x^{n+} exerted on the constriction. The capsule size is $a/\ell_z = 0.2, 0.4, 0.6, 0.7, 0.8, 0.9, 1$.

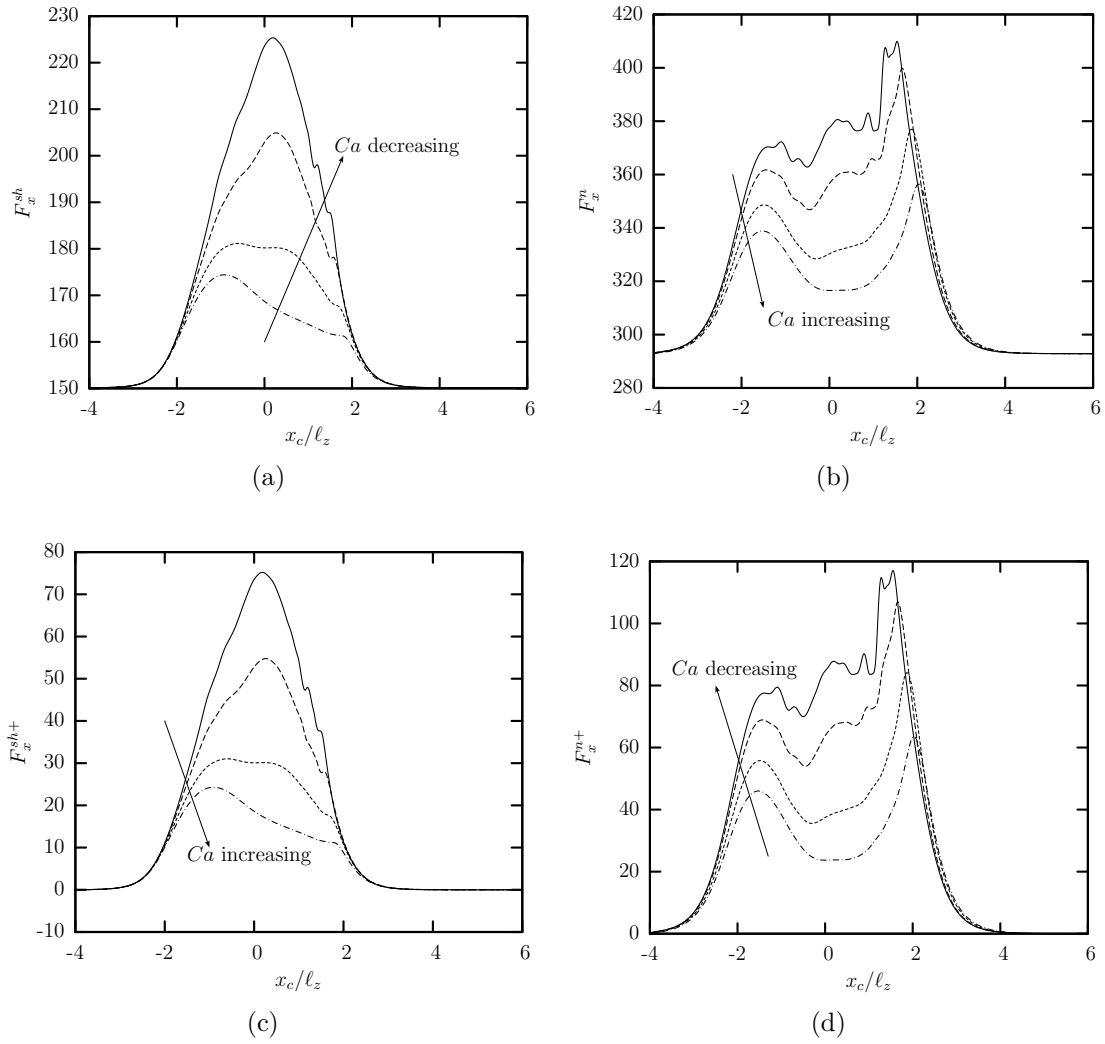

Figure 4.4: Effects of the flow rate Ca on the shear and normal forces on the constriction, for a Skalak capsule with $C = 1$, $\lambda = 1$ and $a/\ell_z = 1$. (a) Shear force F_x^{sh}, (b) normal force F_x^n, (c) additional shear force F_x^{sh+}, and (d) additional normal force F_x^{n+} exerted on the constriction. The flow rate is $Ca = 0.01, 0.02, 0.05, 0.1$.

the constriction and the frontal area of the constriction A_{const},

$$F_x^n \sim \Delta P^{const} A_{const} \tag{4.6}$$

We emphasize that a lower flow rate Ca (or a larger capsule size a) causes higher shear and normal forces exerted on the constriction owing to a higher flow blocking. Following a comparison between our computational results and the scaling analysis, Eqs.(4.5) and (4.6), the higher flow blocking should increase the shear stress τ_{const} and the pressure difference ΔP^{const} on the constriction.

4.4 Effects of viscosity ratio

In this section, we investigate the effects of the viscosity ratio λ on the hydrodynamic forces on the constriction as a capsule passes through the microfluidic constriction. For this, we consider a capsule with a fixed size $a/\ell_z = 0.9$ and flow rate $Ca = 0.1$, while we vary the viscosity ratio in the range $\lambda = 0.01 - 5$, i.e., we investigate from inviscid to very viscous capsules.

Figure 4.5 shows the hydrodynamic force F_x and the additional hydrodynamic force F_x^+ exerted on the constriction for several viscosity ratios. The viscosity ratio has very weak effects on both forces which are positive for all viscosity ratios (even for inviscid capsules with $\lambda \ll 1$).

Figure 4.6 shows the effects of the viscosity ratio on the shear and normal forces on the constriction. As the viscosity ratio λ increases, the shear force F_x^{sh} and the additional shear force F_x^{sh+} increase when the capsule is in the constriction

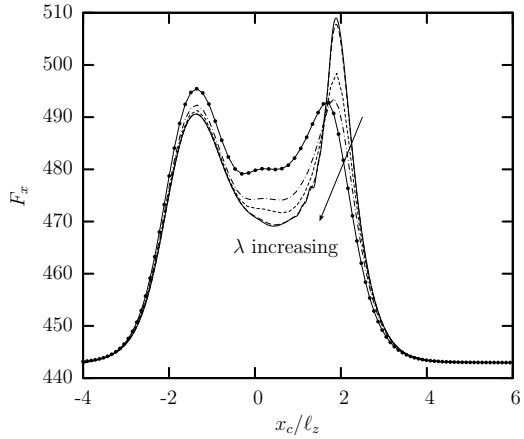

(a)

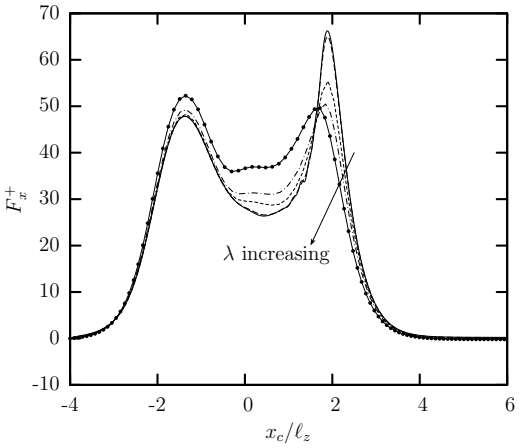

(b)

Figure 4.5: Effects of the viscosity ratio λ on (a) the hydrodynamic force F_x and (b) the additional hydrodynamic force F_x^+ exerted on the constriction as a function of the capsule centroid x_c, for a Skalak capsule with $C = 1$, $Ca = 0.1$ and $a/\ell_z = 0.9$. The viscosity ratio is $\lambda = 0.01, 0.1, 1, 2, 5$.

$(-1 < x/\ell_z < 1)$. Before the constriction, the shear forces are insensitive to the viscosity ratio. The normal force F_x^n and the additional normal force F_x^{n+} are weakly affected by the viscosity ratio λ.

4.5 Comparison with droplet dynamics

In this section, we focus on the effects of the viscosity ratio on the forces exerted on the constriction due to a droplet passing and compare these forces with the forces exerted on the constriction due to a capsule passing.

Figure 4.7 shows the effects of the viscosity ratio on the hydrodynamic forces exerted on the constriction owing to the droplet passing. Both F_x and F_x^+ are more strongly affected by the viscosity ratio than those for the capsule passing as seen in figure 4.5. As the viscosity ratio λ decreases, the hydrodynamic force F_x and the additional hydrodynamic force F_x^+ exerted on the constriction owing to the droplet passing are decreased.

To explain the different effects of the viscosity ratio on the hydrodynamic forces exerted on the constriction owing to the soft particles passing, we need to consider the inner circulation. As discussed in chapter 3, the inner circulation of the droplet is generated owing to the continuity of the interfacial shear stress from the surrounding and inner fluids. Based on table 3.2, the higher viscosity ratio results in a decrease of the droplet is inner circulation. This means that the resistance (i.e., shear and normal stress) at the droplet interface may be increased with increasing the viscosity ratio.

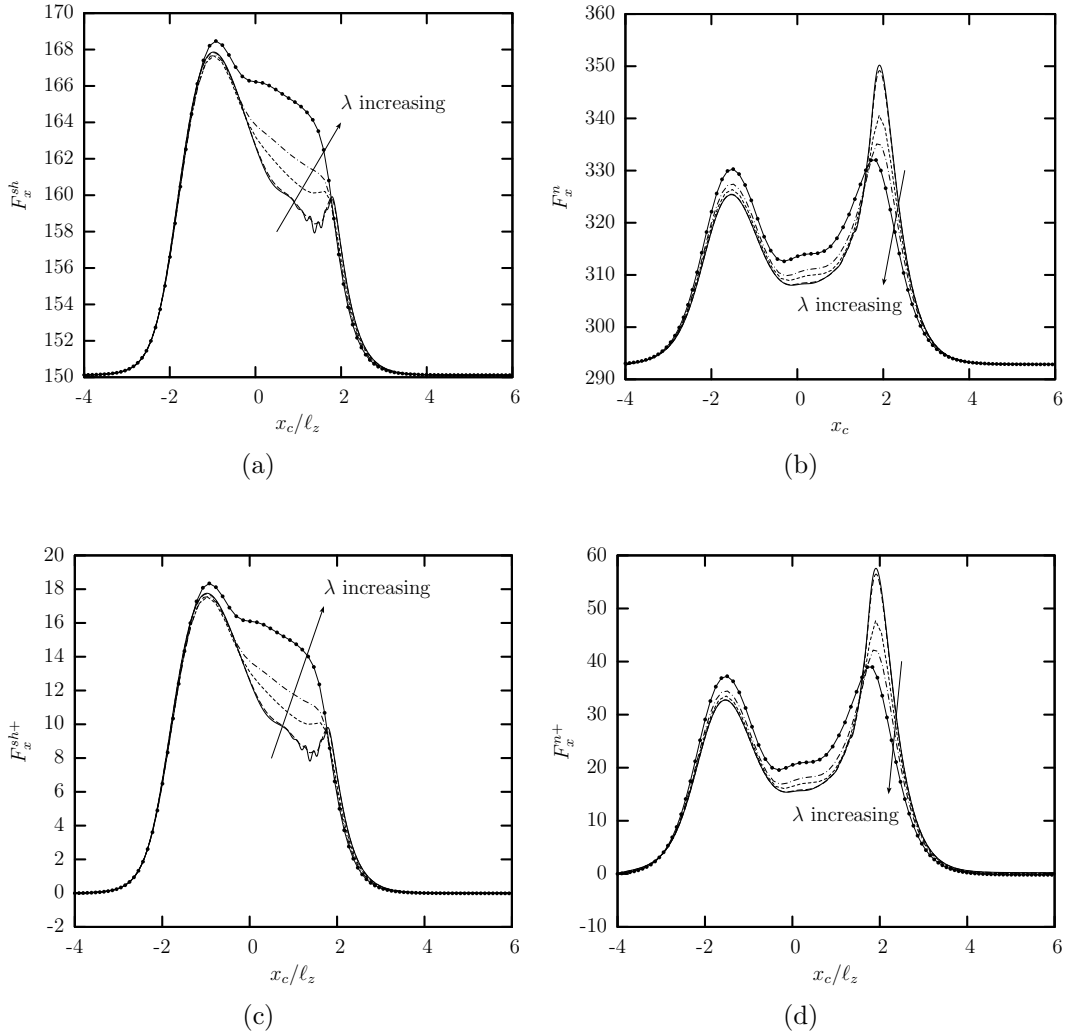

Figure 4.6: Effects of the viscosity ratio λ on the shear and normal forces on the constriction for a Skalak capsule with $C = 1$, $Ca = 0.1$ and $a/\ell_z = 0.9$. (a) Shear force F_x^{sh}, (b) normal force F_x^n, (c) additional shear force F_x^{sh+}, and (d) additional normal force F_x^{n+} exerted on the constriction. The viscosity ratio is $\lambda = 0.01, 0.1, 1, 2, 5$.

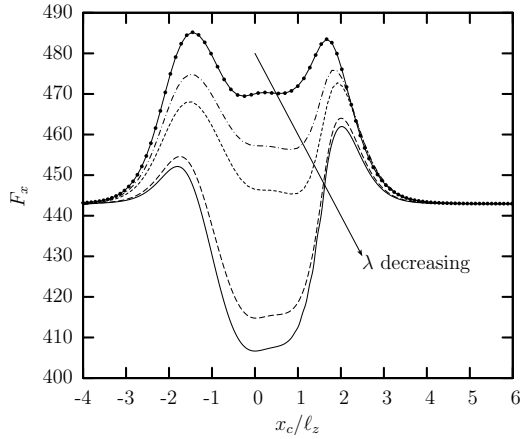

(a)

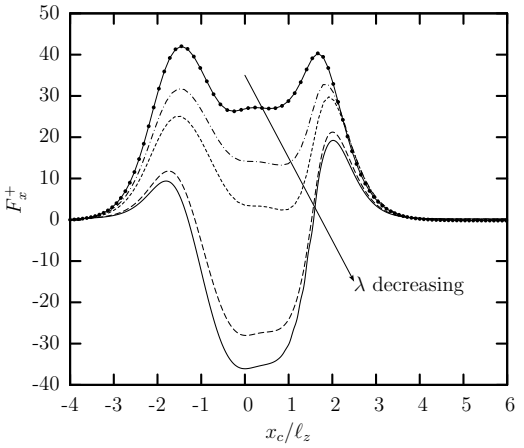

(b)

Figure 4.7: Effects of the viscosity ratio λ on (a) the hydrodynamic force F_x and (b) the additional hydrodynamic force F_x^+ exerted on the constriction as a function of the droplet centroid x_c, for a droplet with $Ca = 0.1$ and $a/\ell_z = 0.9$. The viscosity ratio is $\lambda = 0.01, 0.1, 1, 2, 5$.

To offer further physical insight, utilizing Eqs.(4.4) and (4.5), we derive the scaling for the additional shear force F_x^{sh+} exerted on the constriction owing to the soft particle passing.

$$F_x^{sh+} \sim (\tau_{const} - \tau_{const,0}) S_{const} \tag{4.7}$$

where the constant $\tau_{const,0}$ is the shear stress on the constriction in the absence of the soft particle. We also derive the scale of the additional normal force F_x^{n+} exerted on the constriction owing to the soft particle passing by using Eqs.(4.4) and (4.6),

$$F_x^{n+} \sim (\Delta P^{const} - \Delta P^{const,0}) A_{const} = \Delta P^{c,0+} A_{const} \tag{4.8}$$

where the constant $\Delta P^{const,0}$ is the pressure difference on the constriction in the absence of the soft particle.

For low-viscosity droplets with $\lambda \ll 1$, the resistance on the droplet surface is decreased owing to the strong inner circulation and thus the shear stress τ_{const} and the pressure difference ΔP^{const} exerted on the constriction are decreased. Thus, the additional shear force F_x^{sh+} and the additional normal force F_x^{n+} are negative as shown in figure 4.8(c,d).

For viscous droplets with $\lambda = O(1)$, the shear stress τ_{const} and the pressure difference ΔP^{const} become larger than the undisturbed values since the slower inner circulation increases for the resistance on the droplet surface. Therefore, the additional shear force F_x^{sh+} and the additional normal force F_x^{n+} are positive.

For high-viscosity droplets with $\lambda \gg 1$, the restriction imposed on the droplet

is more increased owing to the much weaker inner circulation. The shear stress τ_{const} and the pressure difference ΔP^{const} continue to increase. Thus, the additional shear force F_x^{sh+} and the additional normal force F_x^{n+} are positive. For a viscosity droplet (e.g. $\lambda = 5$), the resistance over the droplet surface owing to the weaker inner circulation of droplet acts like the restriction imposed by the capsule surface. Thus in this case, the forces are very similar to those for the capsule (at any viscosity ratio) as shown in figures 4.8 and 4.6.

Therefore, our study shows that the forces exerted on the constriction owing to the droplet passing are strongly affected by the viscosity ratio in contrast to those on the constriction owing to the capsule passing.

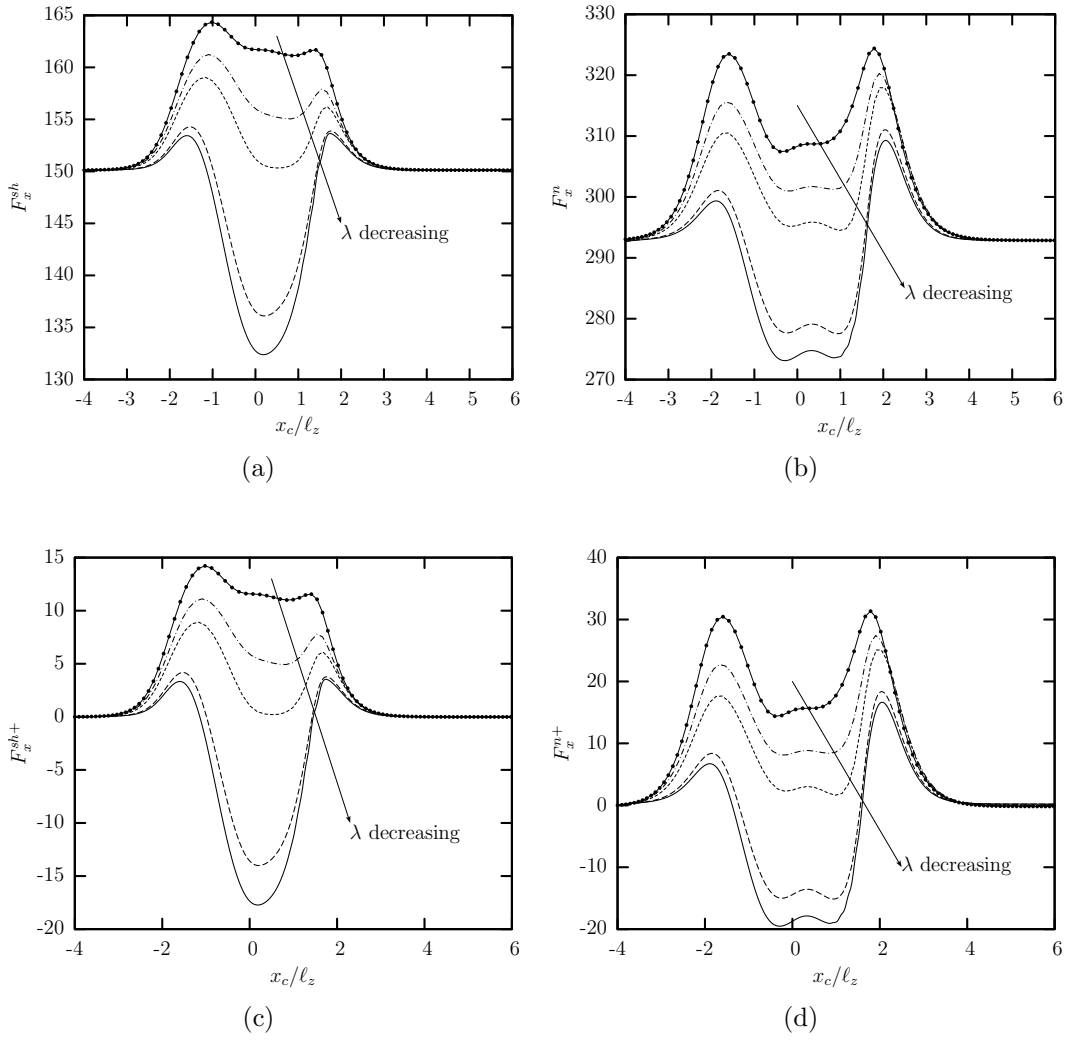

Figure 4.8: Effects of viscosity ratio λ on the shear and normal forces on the constriction for a droplet with $Ca = 0.1$ and $a/\ell_z = 0.9$. (a) Shear force F_x^{sh}, (b) normal force F_x^{n}, (c) additional shear force F_x^{sh+}, and (d) additional normal force F_x^{n+} exerted on the constriction. The viscosity ratio is $\lambda = 0.01, 0.1, 1, 2, 5$.

Chapter 5: Dynamics of an elastic capsule in a square microfluidic constriction

In this chapter, we study the transient dynamics of a capsule flow in square microfluidic constriction. The investigation of capsule deformation and its motion in a square constriction channel has been used in microfluidic devices such as filtration systems, cell sorting or separation system and biomedical devices. Abkarian, Faivre and Stone [1] focused on the motion of red blood cells in a square constriction channel. They investigated the effects of pressure difference on the motion of cells. Leclerc *et al.* [42] studied the transient flow of microcapsules through square constriction channels. They focused on the capsule deformation for varying capsule sizes and computed the capsule shearing modulus from the calculated relaxation time of capsules when the capsule returned back to the initial shape after passing through the constriction. In addition, they compared the calculated the value of the shearing modulus with previous results [44].

Here we numerically investigate the motion of an elastic capsule in a square microfluidic constriction. First, we determine the transient motion of a capsule and its deformation when the capsule passes through the constriction. We demonstrate

the effects of flow rate Ca on the capsule motion in the square constriction. Furthermore, we compare our computational results of the square constriction with our previous results of the rectangular constriction from chapter 3 and 4.

5.1 Problem description

We consider a three-dimensional capsule flowing along the centerline of a square microfluidic constriction with a square constriction in the middle, as shown in figure 5.1. The flow direction (i.e., the x-axis) corresponds to the channel's or capsule's length while the z-direction will be referred as height. The width and height of the constriction are $2\ell_z$ and those of the outer channel are $4\ell_z$. The square constriction has length $2\ell_z$ while the length of the entire microchannel is $20\ell_z$. The half-height of the square constriction ℓ_z is used as the length scale for the present problem. At the time $t = 0$ the capsule is located at $-4\ell_z$, the fluid flow begins inside the microfluidic channel and we investigate the transient dynamics of the capsule as it enters and exists the square constriction $[-\ell_z,\ell_z]$. The velocity is scaled with the average undisturbed velocity $\mathcal{U}$ in the outer square channel and the time is scaled with the $\ell_z/\mathcal{U}$. In addition, the pressure is scaled with $\mu\mathcal{U}/\ell_z$, and the membrane tensions with G_s.

In our work, we consider the exterior and inner fluid as a Newtonian fluids. In addition we assume that the flow rate Q inside the microchannel is fixed. We consider a Skalak capsule with prestress $\alpha_p = 0.05$ and membrane hardness $C = 1$.

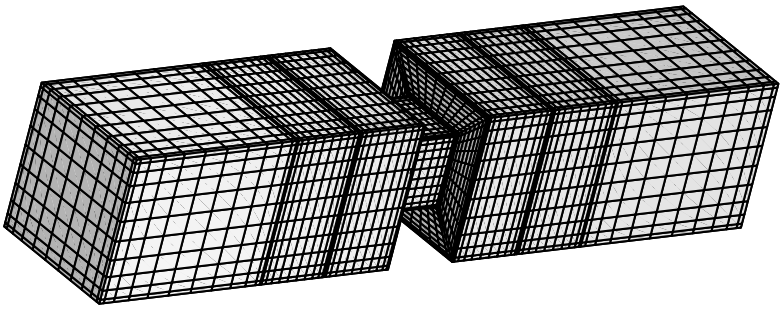

Figure 5.1: Illustration of a square microfluidic constriction with a square constriction in the middle.

5.2 Transient dynamics of the capsule passing through a square microfluidic constriction

In this section, we investigate the transient dynamics of a viscous capsule (with viscosity ratio $\lambda = 1$) as it passes through the square-constricted microfluidic channel. We consider the effects of the flow rate Ca on the capsule motion. Our results, including the capsule lengths, its velocity U_x, the additional pressure difference ΔP^+ and the hydrodynamic forces, are represent as functions of the capsule centroid x_c.

The successive capsule profiles are shown in figure 5.2. Near the entrance of the constriction, the capsule becomes more pointed from the spherical shape into the bullet-like shape as seen in figure 5.2(a). It is due to the strong hydrodynamic forces associated with the cross-sectional area decrease where the average fluid velocity is increased inside the constriction since the flow rate Q is fixed in the study.

Thus as the capsule approaches the constriction, its length L_x is increased while its height L_z and width L_y (where $L_y = L_z$ for this problem owing to symmetry) are decreased as seen in figure 5.3.

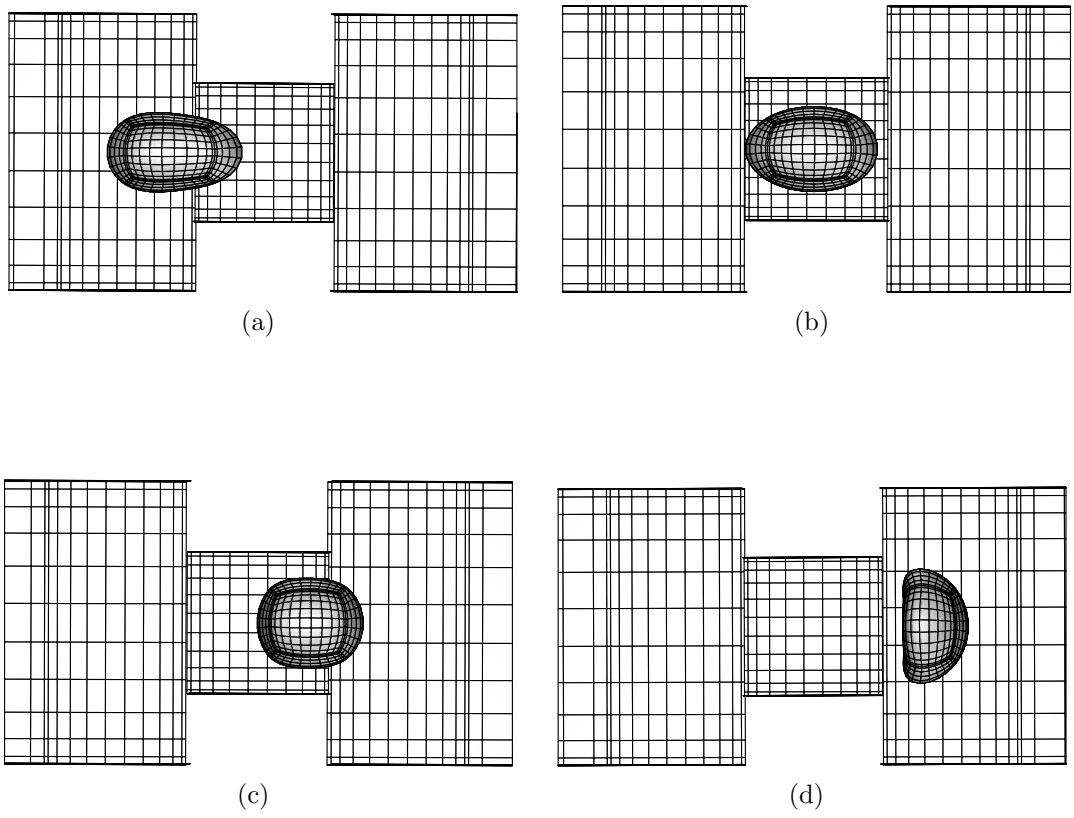

Figure 5.2: The shape of a Skalak capsule with $C = 1$, $a/\ell_z = 0.7$, $\lambda = 1$ and $Ca = 0.1$ moving inside the square microfluidic constriction. The capsules centroid x_c/ℓ_z is (a) -1.34, (b) -0.06, (c) 0.71, and (d) 1.73. The three-dimensional capsule views were derived from the actual spectral grid using orthographic projection in plotting.

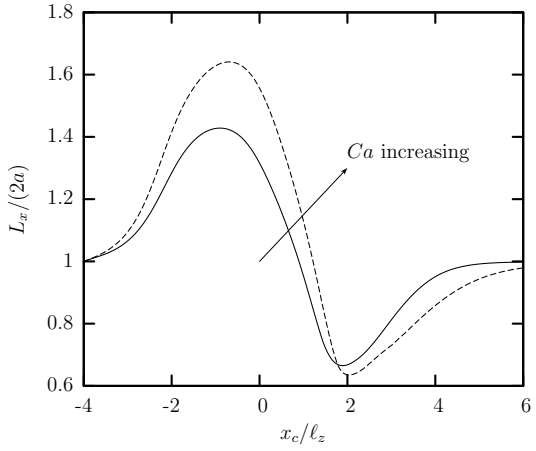

(a)

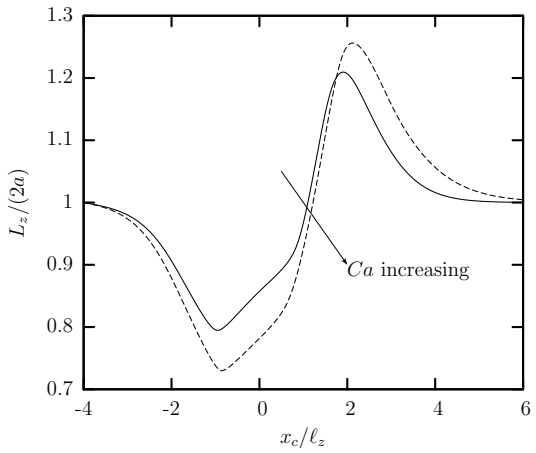

(b)

Figure 5.3: The capsule lengths as a function of the centroid x_c, for a Skalak capsule with $C = 1$, $a/\ell_z = 0.7$ and $\lambda = 1$, for flow rate $Ca = 0.1, 0.2$. (a) Length L_x and (b) height L_z (scaled with the length $2a$ of the undisturbed spherical shape). These lengths are determined as the maximum distance of the interface in the x and z directions.

When the capsule approaches nearly the middle of the constriction as in figure 5.2(b), the capsule has obtained a shape similar to the elliptical shape. The capsule elongates in the flow direction and decreases in the lateral and its height direction, as shown in figure 5.3.

As the capsule moves out of the constriction as seen figure 5.2(c), the downstream portion of the capsule slows down owing to the cross-section expansion, i.e., the sudden decrease of the average fluid velocity, while the upstream part of the capsule still advances with the constriction flow velocity. Both actions causes a compression of the capsule and a significant reduction of the capsule length L_x associated with a fast increase of the capsule width L_y and height L_z as shown in figure 5.3. When the capsule completely exits the constriction, the capsule lateral expansion is much more pronounced where it obtains a parachute-like shape as seen in figure 5.2(d). When the capsule has the parachute-like shape, the capsule has the maximum values of height L_z and width L_y. After that, the capsule returns back to a bullet shape in the outer square channel.

Therefore, the two different sizes of the microchannel, i.e., confinement and expansion, cause two distinct interfacial shapes. In the constriction, the capsule length L_x has the maximum value and its width L_y and height L_z have the minimum value where the capsule obtains a bullet shape. The opposite happens after the capsule obtains a parachute-like shape where the capsule length L_x has the minimum value and its width L_y and height L_z have the maximum value. Similar phenomena has been observed in chapter 3 in a rectangular constriction.

Figure 5.5 shows the effects of the flow rate Ca on the tip curvatures of the

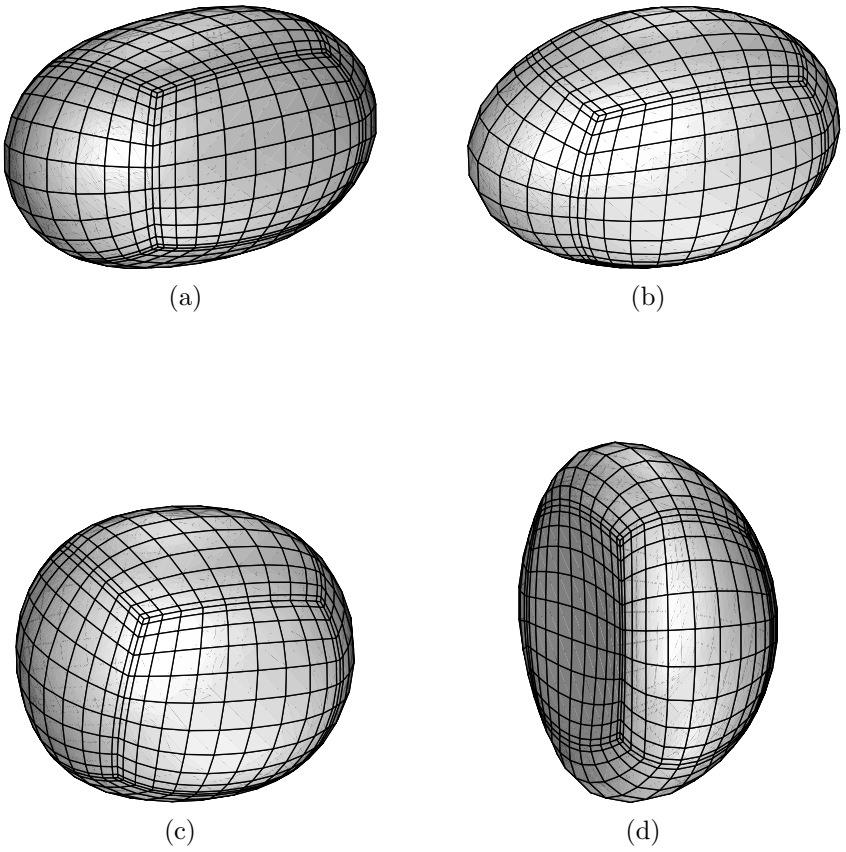

Figure 5.4: The shape of a Skalak capsule with $C = 1$, $a/\ell_z = 0.7$, $\lambda = 1$ and $Ca = 0.1$ moving inside the microfluidic constriction, for capsules centroid (a) $x_c/\ell_z = -1.34$, (b) $x_c/\ell_z = -0.06$, (c) $x_c/\ell_z = 0.71$ and (d) $x_c/\ell_z = 1.73$. The capsule shape is plotted as seen slightly askew from the positive z-axis to reveal its fully three-dimensional conformation.

capsule. When the capsule approaches the constriction, the curvature $\mathcal{C}_{xz}^{f}$ on the front tip increases while the curvature $\mathcal{C}_{xz}^{b}$ of the back tip decreases where the capsule becomes a bullet-like shape as shown in figure 5.4(a). When the capsule is in the middle of the constriction, the curvature $\mathcal{C}_{xz}^{f}$ has the maximum value while the curvature $\mathcal{C}_{xz}^{b}$ continues to decrease. This means that the capsule becomes more pointed along the flow direction since the capsule deformation is limited along the height or width direction. As the capsule moves out of the constriction completely, the tip curvature $\mathcal{C}_{xz}^{b}$ tends to be negative where the upstream edge of the capsule changes its shape from a convex to a concave as shown in figure 5.4(d). The tip curvature $\mathcal{C}_{xz}^{b}$ has the minimum value due to the maximum expansion of the downstream edge of the capsule. As the flow rate Ca increases, the curvatures have a higher values since the capsule is more deformed owing to the strong hydrodynamic force.

To provide more information on the motion of the elastic capsule in the square constricted microchannel, in figure 5.6(a) we present the variation of the capsule surface area S_c with the flow rate Ca. The capsule surface area S_c is increased when the capsule squeezes before the constriction while it is reduced after the capsule passing through the constriction. When the flow rate Ca increases, the capsule has a larger surface area S_c owing to the stronger forces.

The same pattern is valid for the maximum τ_{max}^{P} and minimum τ_{min}^{P} principal tension over the capsule surface for several flow rates Ca as shown in figure 5.6(b,c). Near the entrance of the constriction as in figure 5.2(a), the maximum principal tension τ_{max}^{P} occurs at the top surface of the capsule, and the minimum principal

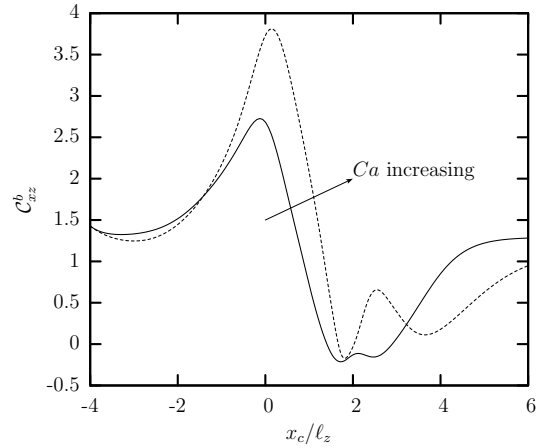

(a)

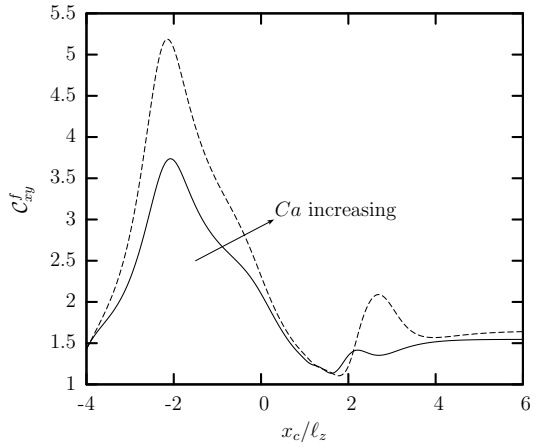

(b)

Figure 5.5: The capsule curvatures as a function of the centroid x_c, for a Skalak capsule with $C = 1$, $a/\ell_z = 0.7$ and $\lambda = 1$, for size $Ca = 0.1, 0.2$. (a) The tip curvature of the back side of the capsule $\mathcal{C}^b_{xz}$ and (b) the tip curvature of the front side of the capsule $\mathcal{C}^f_{xz}$, at the intersection of the capsule surface with the $y = 0$ plane.

tension τ^P_{min} is initially located at the back side of the capsule, e.g. left-side of the capsule. Thus, the capsule elongates along the flow direction. When the capsule is in the constriction as in figure 5.2(b,c), the maximum principal tension τ^P_{max} maintains a high value until the capsule exits the constriction completely while the minimum principal tension τ^P_{min} becomes negative. The maximum principal tension τ^P_{max} continues to be located at at the top surface of the capsule. In contrast, the location of the minimum principal tension τ^P_{min} is changed from the front side of the capsule to the lateral side of the capsule. As the capsule moves out of the constriction completely as seen figure 5.2(d), the minimum principal tension τ^P_{min} has the minimum value where the capsule obtains a parachute-like shape. The negative tension causes local compression. The maximum principal tension τ^P_{max} decreases. It is located at the downstream of the capsule. As the flow rate Ca increases, the maximum principal tension on the capsule surface increases owing to the stronger hydrodynamic forces. The location of the minimum and maximum tensions on the capsule surface has the same trend for the different flow rates.

The lower flow rate Ca (or higher flow blocking) results in a decrease of the capsule velocity U_x and an increase of the additional pressure difference ΔP^+, owing to the narrow gap h between the capsule surface and the solid wall as seen in figure 5.7. As discussed in chapter 3, we analyze the variation of the capsule velocity U_x and the additional pressure difference ΔP^+ with the flow rate Ca by utilizing the scaling behavior presented in Eqs.(19) and (27) from in Kuriakose and Dimitrakopoulos [37]. The capsule velocity inside the constriction should scale proportionally with the gap

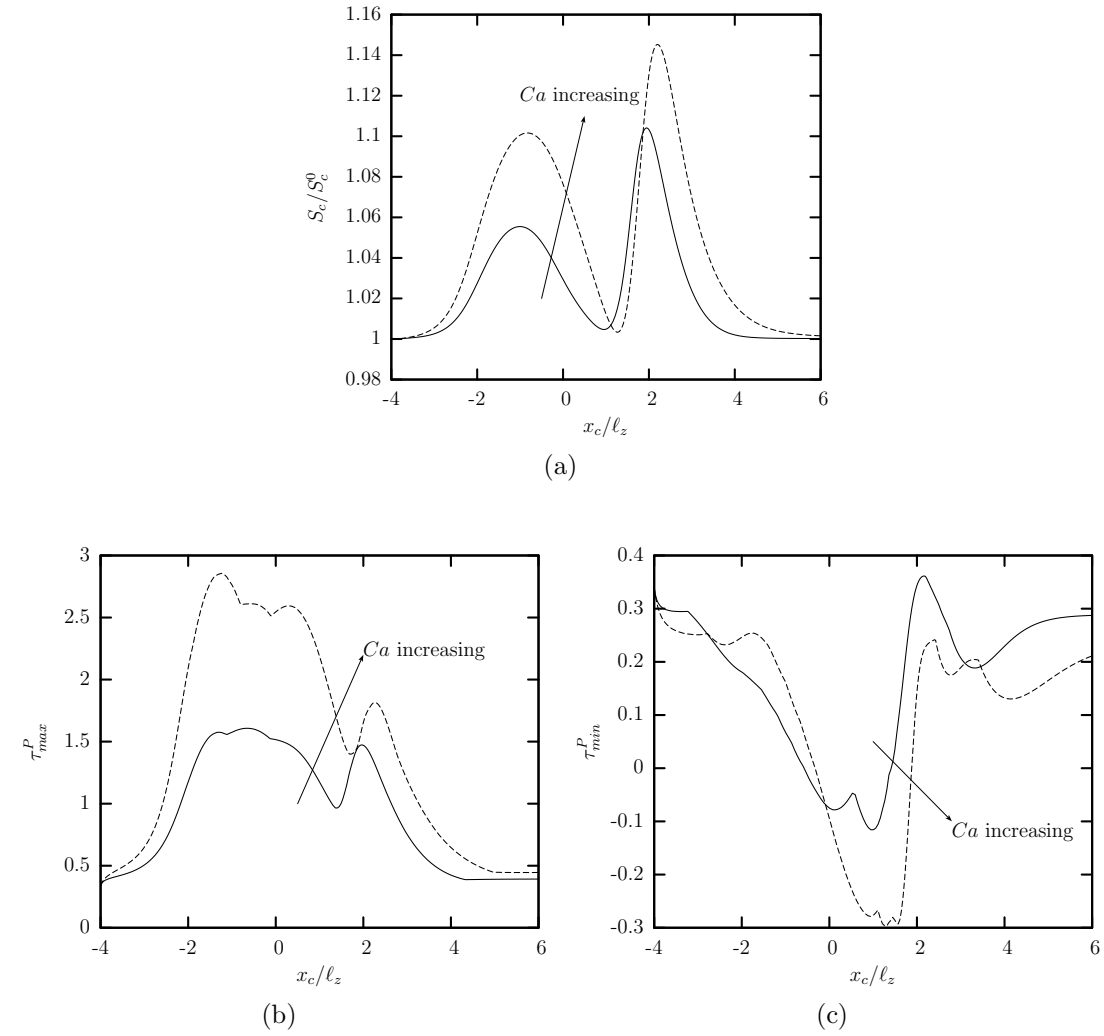

Figure 5.6: The surface area and principal tensions as a function of the centroid x_c, for a Skalak capsule with $C = 1$, $a/\ell_z = 0.7$ and $\lambda = 1$, for flow rate $Ca = 0.1, 0.2$. (a) Surface area of the capsule S_c (scaled with the capsule surface area S_c^0), (b) maximum principal tension τ^P_{max}, and (c) minimum principal tension τ^P_{min} on the capsule.

h between the capsule surface and the solid walls,

$$\frac{U_x - \mathcal{U}}{\mathcal{U}} \sim \frac{h}{\ell_z} \tag{5.1}$$

where $\mathcal{U}$ is the average undisturbed velocity in the square constriction and ℓ_z the half-size of the square constriction. The additional pressure difference should be inversely proportional to the gap,

$$\frac{\Delta P^+}{\Pi} \sim \frac{\ell_z}{h} \tag{5.2}$$

where Π is the pressure scale in the outer square channel. As the flow rate Ca decreases, the gap h between the capsule surface and the solid wall decreases, and thus the capsule velocity U_x decreases while the additional pressure difference ΔP^+ increases, in agreement with our computational results seen in figure 5.7.

Figure 5.8 shows the hydrodynamic force F_x and the additional hydrodynamic force F_x^+ exerted on the square constriction owing to the capsule passing for two flow rates. When the capsule is near the constriction, the hydrodynamic force increases owing to higher flow blocking between the capsule surface and the solid walls caused from the decrease of the cross-sectional area. As the capsule moves out of the constriction completely, the hydrodynamic force increases owing to the flow blocking associated with the capsule expansion. The additional hydrodynamic force F_x^+ has the same trend as for the hydrodynamic force F_x. As the flow rate Ca decreases, both forces are increased owing to the narrower gap h between the

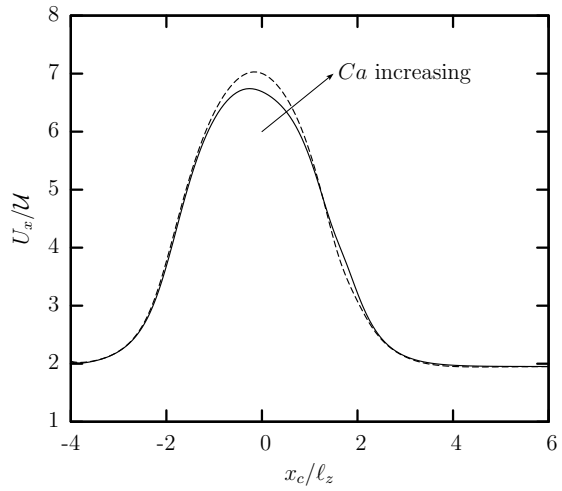

(a)

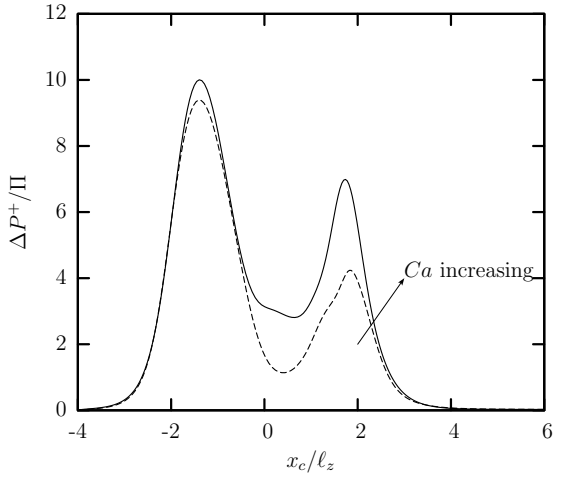

(b)

Figure 5.7: Capsule properties as a function of the centroid x_c. (a) The capsule velocity U_x, and (b) the additional pressure difference ΔP^+ for a Skalak capsule with $C = 1$, $a/\ell_z = 0.7$ and $\lambda = 1$, for flow rate $Ca = 0.1, 0.2$.

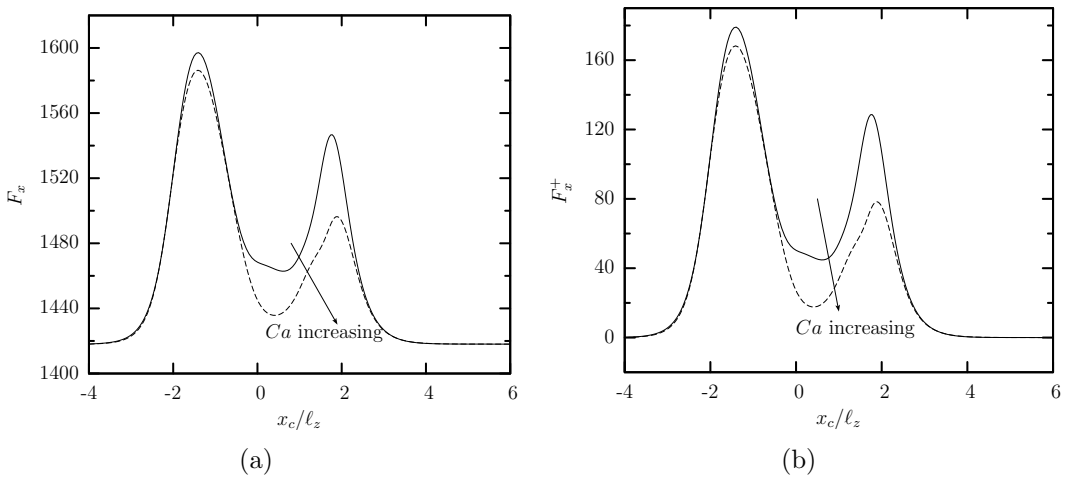

Figure 5.8: The hydrodynamic forces on the square constriction as a function of the capsule centroid x_c, for a Skalak capsule with $C = 1$, $a/\ell_z = 0.7$ and $\lambda = 1$. Effects of the flow rate Ca on (a) the hydrodynamic force F_x and (b) the additional hydrodynamic force F_x^+ exerted on the constriction. The flow rate is $Ca = 0.1, 0.2$.

capsule surface and the solid wall and thus the higher flow blocking.

Figure 5.9 shows the shear and normal forces on the square constriction owing to the capsule passing. The shear force F_x^{sh} and normal force F_x^n increase near the constriction, where the cross-sectional area decreases, owing to the higher flow blocking. As the capsule moves out of the constriction completely, the normal force F_x^n is much higher than the shear force F_x^{sh}. The additional shear force F_x^{sh+} and normal force F_x^{n+} have the same trend for the regular forces. As the flow rate Ca increases, the forces are decreased owing to the larger gap h between the capsule surface and the solid wall. Following a comparison between our computational results and Eqs.(4.5) and (4.6), the higher flow blocking should increase the shear stress τ_{const} and the pressure difference ΔP^{const} on the constriction presented in

Eq.(4.6) in chapter 4.

5.3 Comparison with the rectangular constricted microchannel

In this section, we clarify the similarities and differences of the capsule transient dynamics passing through the rectangular and square constrictions. To investigate the effects of the constriction type (i.e., a rectangular or a square shape) on the capsule dynamics, we consider the capsule size $a/\ell_z = 0.7$, flow rate $Ca = 0.1$, viscosity ratio $\lambda = 1$, and membrane hardness $C = 1$.

A comparison of the capsule deformation, as shown in figure 5.10, reveals that the capsule's length L_x and height L_z deform similarly as the capsule passes through both constrictions. In both constrictions, the capsule deformation is strongly affected by the hydrodynamic forces owing to the significant changes in the flow rate caused by the constriction. However, the capsule is more deformed in the square constriction owing to the stronger hydrodynamic forces since the cross-section area of the square constriction is half that of the rectangular constriction. The capsule's width L_y in the square channel shows the same deformation trend with its height L_z owing to the symmetry of the constriction, as seen in figure 5.10(b). In the rectangular constriction, the capsule width L_y deforms significantly along the less-confined lateral direction of the channel cross-section (i.e., the channel width) to facilitate the development of strong lateral tensions required for interfacial stability as discussed in Kuriakose and Dimitrakopoulos [37].

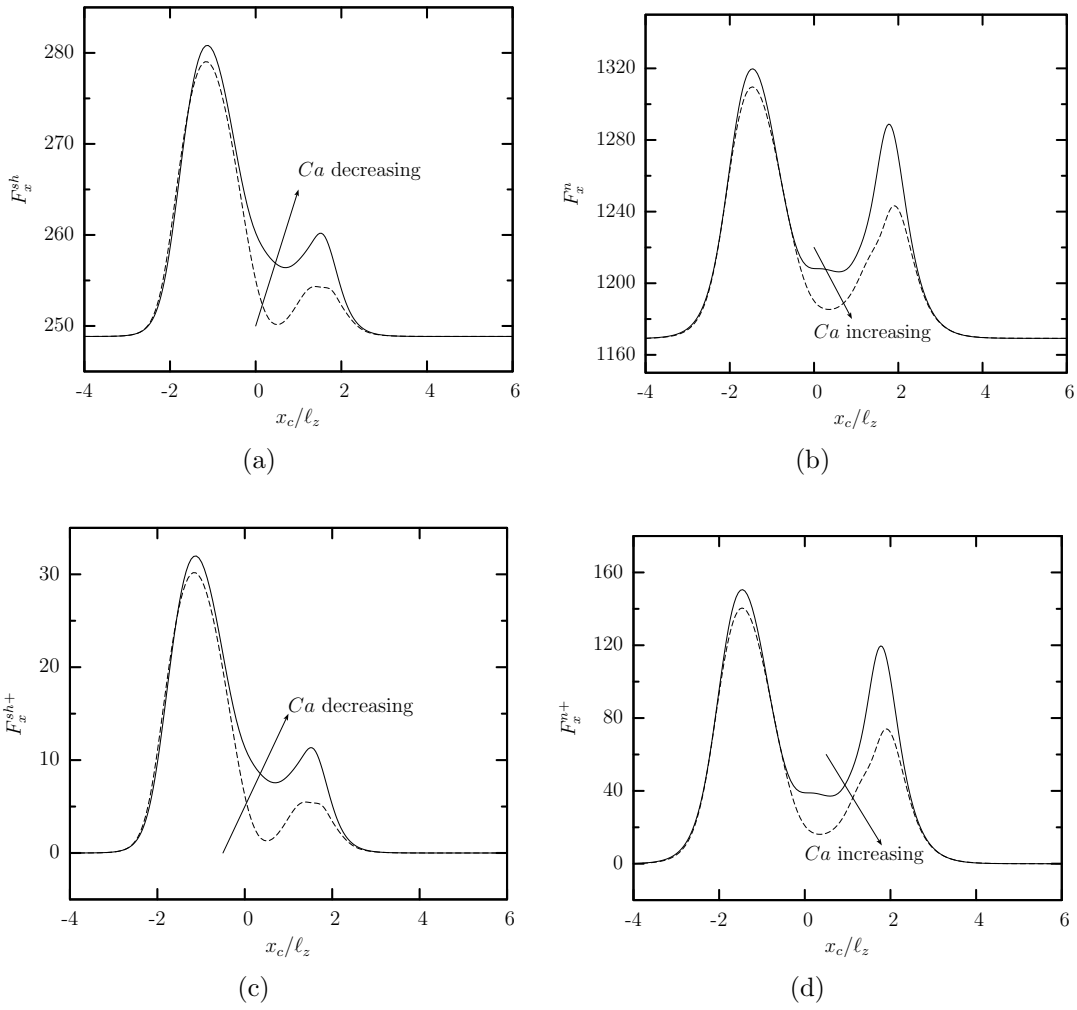

Figure 5.9: Effects of the flow rate Ca on the shear and normal forces on the constriction for a Skalak capsule with $C = 1$, $a/\ell_z = 0.7$ and $\lambda = 1$. (a) Shear force F_x^{sh}, (b) normal force F_x^n, (c) additional shear force F_x^{sh+}, and (d) additional normal force F_x^{n+} exerted on the constriction. The flow rate is $Ca = 0.1, 0.2$.

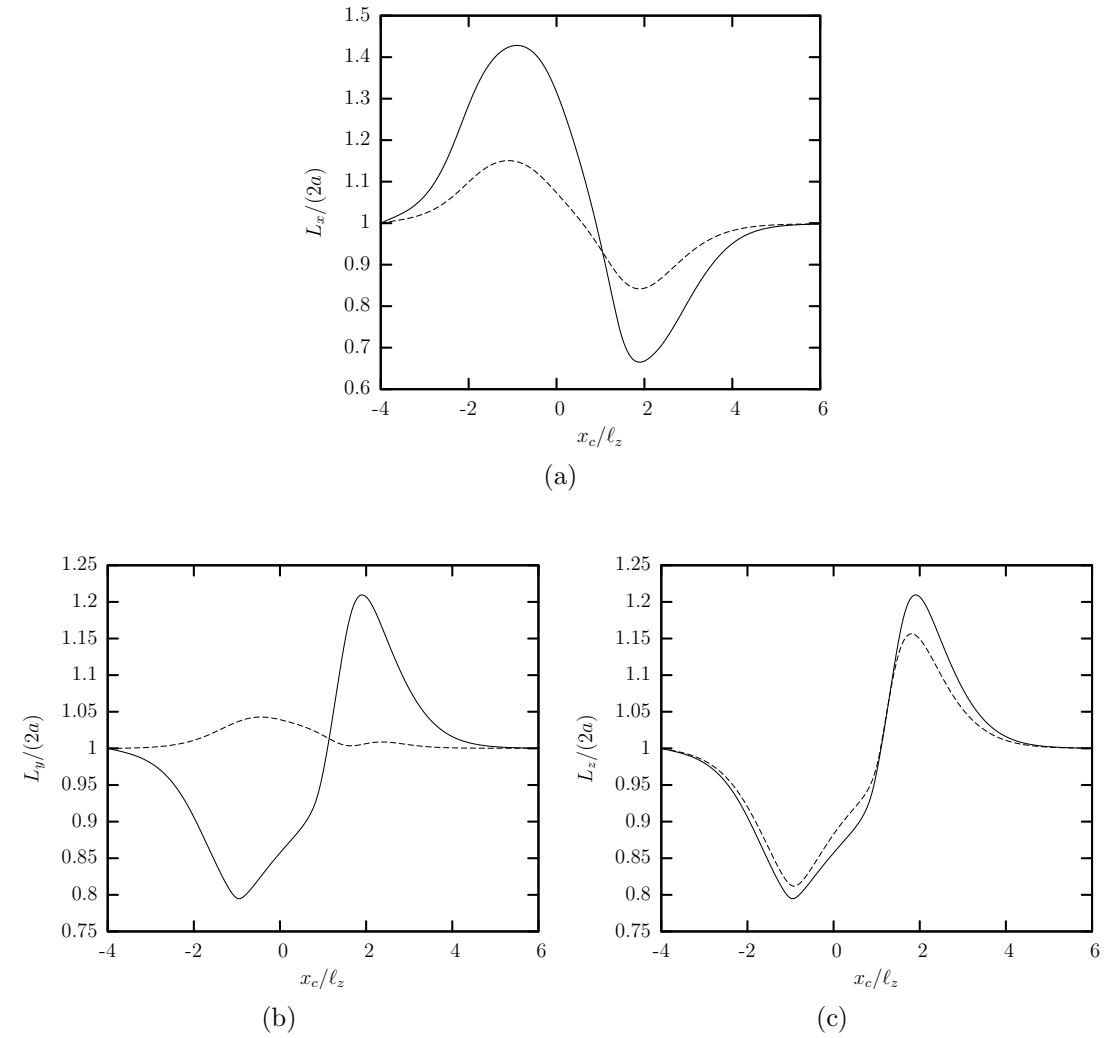

Figure 5.10: Effects of the constriction type on the capsule lengths as a function of the centroid x_c, for a Skalak capsule with $C = 1$, $a/\ell_z = 0.7$, $\lambda = 1$ and $Ca = 0.1$. (a) Length L_x, (b) width L_y and (c) height L_z (scaled with the length $2a$ of the undisturbed spherical shape). The solid line represents the square constriction while the dashed line represents the rectangular constriction.

A comparison of the capsule velocity U_x and additional pressure difference ΔP^+ in the two constriction types is shown in figure 5.11. The capsule velocity increases near the constriction, while the maximum velocity is achieved in the middle of the constriction for both types. The additional pressure difference increases when the capsule is squeezed before entering the constriction or expanded after passing the constriction. However, the capsule velocity and the additional pressure difference are higher in the square constriction owing to the higher hydrodynamic forces caused by the significant changes of the flow rate in this type of constriction.

For the case of the hydrodynamic forces exerted on the constriction as the capsule passes, the forces increase when the capsule is compressed or expanded near the constriction. As seen in figure 5.12, they have a similar trend for both constriction types. However, in the square constriction, the forces are much larger than those in the rectangular constriction owing to the strong flow blocking as shown in figure 5.12. Following a comparison between our computational results and the scaling analysis, Eqs.(4.5) and (4.6), the higher flow blocking should increase the shear stress τ_{const} and the pressure difference ΔP^{const} on the square constriction.

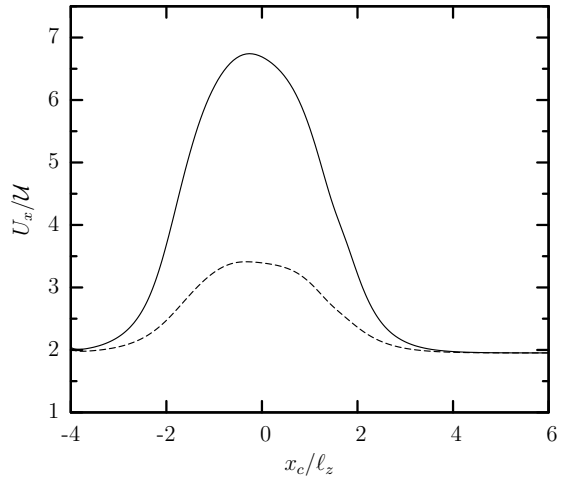

(a)

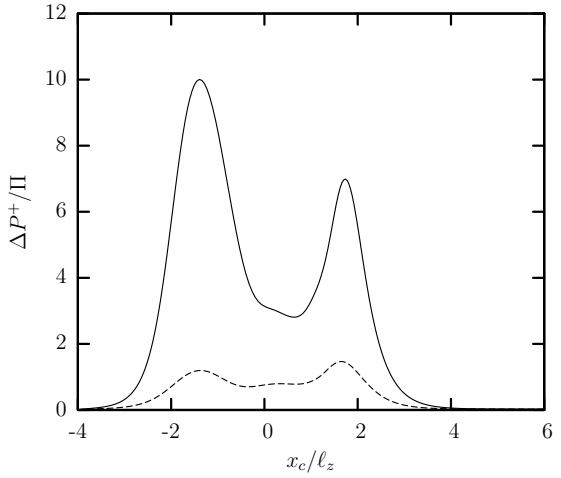

(b)

Figure 5.11: Effects of the constriction type on capsule properties as a function of the centroid x_c, for a Skalak capsule with $C = 1$, $a/\ell_z = 0.7$ and $\lambda = 1$, for flow rate $Ca = 0.1$. (a) The capsule velocity U_x, and (b) the additional pressure difference ΔP^+ The solid line represents the square constriction while the dashed line represents the rectangular constriction.

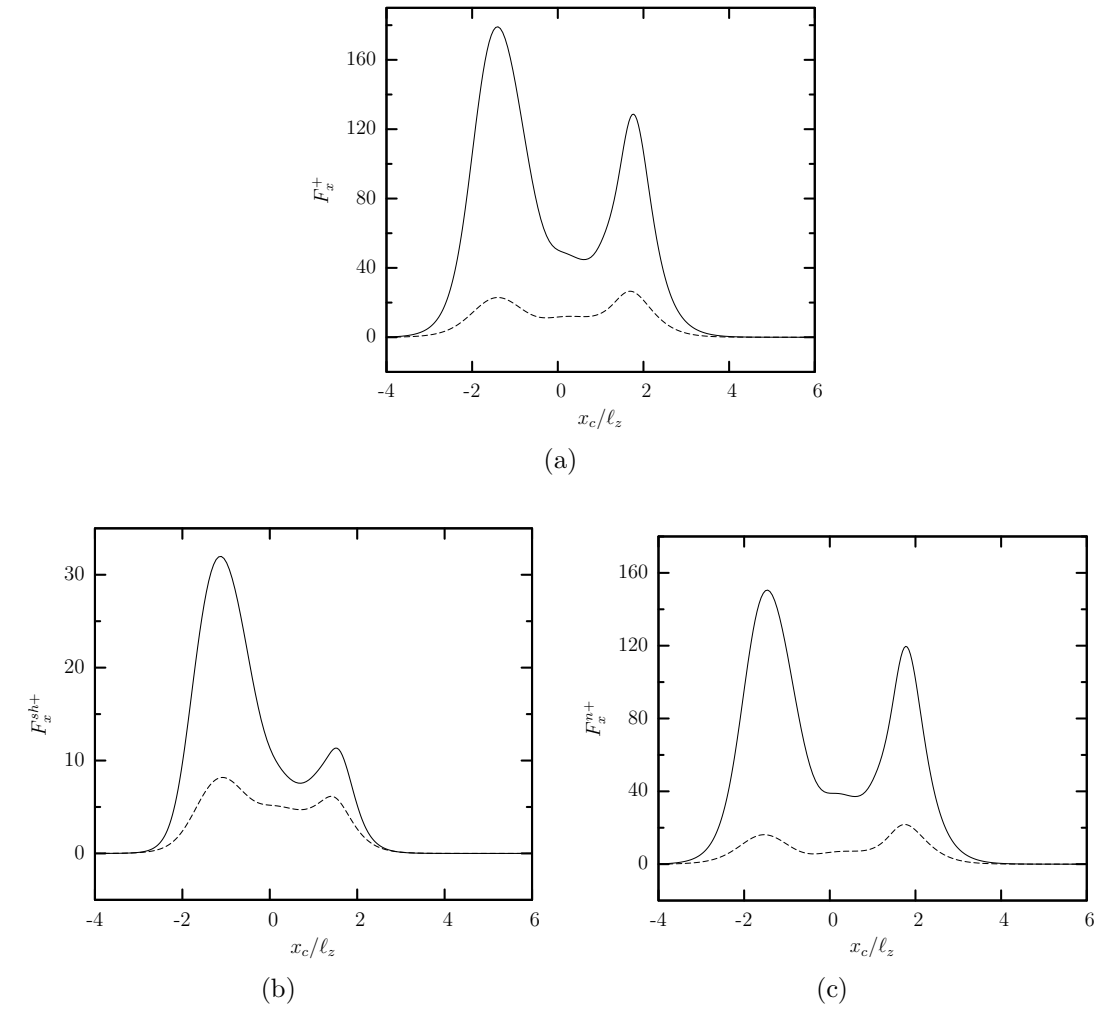

Figure 5.12: Effects of the constriction type on the forces on the constriction for a Skalak capsule with $C = 1$, $a/\ell_z = 0.7$, $Ca = 0.1$ and $\lambda = 1$. (a) Additional force F_x^+, (b) additional shear force F_x^{sh+}, and (c) additional normal force F_x^{n+} exerted on the constriction owing to the caspule passing. The solid line represents the square constriction while the dashed line represents the rectangular constriction.

Chapter 6: Conclusions

In this dissertation, we have investigated computationally the transient dynamics of an elastic capsule flowing along the centerline of microfluidic constricted channels. We have studied a slightly over-inflated elastic capsule made of a strain-hardening membrane (following the Skalak et al. constitutive law) with comparable shearing and area dilatation resistance.

In chapter 3, we considered a square microchannel with a rectangular constriction. Our investigation involves low-to-moderate flow rates with capillary number $Ca = O(0.1)$ and capsule sizes a comparable or smaller to the constriction height. This study is motivated by a wide range of applications including drug delivery, cell sorting and cell characterization devices, microcapsule fabrication, determination of membrane properties, and of course its similarity to blood flow in vascular capillaries.

Our computational investigation reveals that the capsule shows a rich deformation behavior as it moves inside the microfluidic device. In particular, the two distinct regimes associated with the microfluidic constriction, i.e., confinement and expansion, result in two distinct interfacial shapes. In the confinement regime, the capsule obtains an elongated shape with a maximum length and a minimum height.

The opposite happens during the expansion dynamics where the capsule obtains a flattened parachute shape.

The deformation of the capsule's length and height is a pure hydrodynamic effect due to the significant changes in the flow caused by the constriction, and thus it is similar to that for a droplet or a vesicle [10, 50]. However, over the entire passing through the rectangular constriction, the capsule shows an elongated width owing to the development of strong lateral tensions on the capsule membrane required for interfacial stability in asymmetric channels as discussed in Kuriakose and Dimitrakopoulos [38]. Therefore, the transient capsule motion is associated with a highly non-axisymmetric, fully three-dimensional capsule shape which cannot be described from single-view observations as commonly happens in microfluidic experiments or based on axisymmetric or two-dimensional computations.

As the capsule size increases (or as the flow rate decreases), the gap between the capsule surface and the solid walls decreases, and thus the capsule velocity decreases while the additional pressure difference increases. Thus, larger capsules take more time to pass the constriction and cause higher additional pressure difference, owing to higher flow blocking.

Our work highlights the effects of two different mechanisms for capsules non-tank-treading transient dynamics. The capsule deformation results from the combined effects of the surrounding and inner fluids normal stresses on the soft particles interface, and thus when the capsule viscosity increases, its transient deformation decreases, as for droplets. However, the capsule deformation is not able to create a strong enough inner circulation (owing to restrictions imposed by the material mem-

brane), and thus the viscosity ratio does not affect much the capsule velocity and the additional pressure difference. In addition, the weak inner circulation results in a positive additional pressure difference even for low-viscosity capsules. This is in direct contrast to low viscosity droplets where the continuity of the interfacial shear stresses from the surrounding and inner fluids creates a strong inner circulation and a negative additional pressure difference. In essence, owing to the weak inner circulation, during transient non-tank-treading motion, capsules at any viscosity ratio λ correspond to high viscosity ($\lambda \gg 1$) droplets, as at steady state where there is no flow inside the capsules [37, 38].

In chpater 4, we focused on the hydrodynamic forces exerted on the constriction owing to the capsule passing with considering different capsule sizes, flow rates and viscosity ratios. As the capsule size increases (or as the flow rate increases), the forces increase owing to higher flow blocking. We note that the forces are only weakly affected by the viscosity ratio. In contrast to the capsule, the forces exerted on the constriction owing to the droplet passing is strongly affected by the viscosity ratio. For low-viscosity droplets, the additional forces are negative owing to the strong inner circulation. For very viscous droplets, the forces exerted on the constriction due to the droplet passing are similar to those due to the capsule passing.

In chapter 5, in addition, we investigated the effects of the constriction type (i.e., rectangular or square constriction) for the capsules non-tank-treading transient dynamics. In the square constriction, the capsule is much more deformed owing to the more change of the flow associated with the smaller cross-section area of the

constriction than that of the rectangular constriction. The capsule becomes more pointed in the square channel. In the rectangular constriction, the capsule prefers to deform along the less-confined lateral direction of the channel, and thus the width L_y has different size with its height L_z. On th other hand, in the square channel, the capsule's width L_y is the same with its height L_z owing to the symmetry of the constriction. As the flow rate increases, the gap between the capsule surface and the solid walls is more increased, the capsule velocity increases while the additional pressure difference and the hydrodynamic forces decrease. In the square constriction, the capsule has much faster velocity and higher the additional pressure difference and the hydrodynamic force than those of the rectangular constriction owing to higher flow blocking caused by the narrower width of the constriction.

It is of interest to note that our conclusions are not restricted to artificial capsules but should also represent physiological capsules, such as erythrocytes, for the same physical reasons. The erythrocyte membrane consists of an outer lipid bilayer (which is essentially a two dimensional incompressible fluid with no shearing resistance as in vesicles) and an underlying spectrin skeleton (which exhibits shearing and area-dilatation resistance like the elastic membrane of common artificial capsules) [71]. Under different flow conditions, the spectrin cytoskeleton dominates the erythrocyte dynamics and the cell behaves like a non-spherical capsule. The erythrocyte is responsible for exchanging oxygen and carbon dioxide with the tissues in the vascular capillaries [55]. The cells interior is a concentrated solution of the protein hemoglobin which binds oxygen in the pulmonary system, and releases it to the tissues throughout the systemic circulation. Because of hemoglobin, the cytoplasm

viscosity is several times higher than the plasma viscosity resulting in a viscosity ratio $\lambda = 5$ at the human body temperature of 37^oC [48, 71]. Our work suggests that the much higher cytoplasmatic viscosity does not affect adversely the velocity of non-tank-trading erythrocytes in vascular capillaries nor impose any additional energy requirement for the cells flow since it does not affect much the additional pressure difference.

Bibliography

[1] M. Abkarian, M. Faivre and H. A. Stone, High-speed microfluidic differential manometer for cellular-scale hydrodynamics. *Proc. Natl. Acad. Sci.* **103**, 538–542 (2006).

[2] A. Alexeev and A. C. Balazs, Designing smart systems to selectively entrap and burst microcapsules. *Soft Matter* **3**, 1500–505 (2007).

[3] A. Alexeev, R. Verberg, and A. C. Balazs, Patterned Surfaces Segregate Compliant Microcapsules. *Langmuir* **23**, 983–987 (2007).

[4] J. P. Arata and A. Alexeev, Designing microfluidic channel that separates elastic particles upon stiffness. *Soft Matter* **5**, 2721–2724 (2009).

[5] A.M. Artolia, A. Sequeiraa, A. S. Silva-Herdadeb and C. Saldanhab, Leukocytes rolling and recruitment by endothelial cells: Hemorheological experiments and numerical simulations. *Journal of Biomechanics* **40**, 3493–3502 (2007).

[6] M. Antia, T. Herricks and P. K. Rathod, Microfluidic modeling of cell-cell interactions in malaria pathogenesis. *PLoS Pathog* **3**, 0939–0948 (2007).

[7] P. Bagchi, Mesoscale simulation of blood flow in small vessels. *Biophys. J.* **92**, 1858–1877 (2007).

[8] D. Barthès-Biesel, A. Diaz and E. Ehenin, Effect of constitutive laws for two-dimensional membranes on flow-induced capsule deformation. *J. Fluid Mech.* **460**, 211–222 (2002).

[9] D. Barthès-Biesel and J. M. Rallison, The time-dependent deformation of a capsule freely membranes on flow-induced capsule deformation. *J. Fluid Mech.* **113**, 251–267 (1981).

[10] S. Braunmüller, L. Schmid and T. Franke, Dynamics of red blood cells and vesicles in microchannels of oscillating width. *J. Phys.: Condens. Matter* **23**, 184116 (2011).

[11] M. Carin,D. Barthès-Biesel, F. Edwards-Lévy, C. Postel, and D. C. Andrei, Compression of biocompatible liquid-filled HSA-alginate capsules: determination of the membrane mechanical properties. *Biotech. Bioeng.* **82**, 207–212 (2003).

[12] M. Chabert and J.-L. Viovy, Microfluidic high throughput encapsulation and hydrodynamic self-sorting of single cells. *Proc. Natl. Acad. Sci.* **105**, 3191–3196 (2008).

[13] W. Chen, Y. Yang, C. Rinadi, D. Zhou and A. Q. Shen, Formation of supramolecular hydrogel microspheres via microfluidics. *Lab on a Chip* **9**, 2947–2951 (2009).

[14] K. V. Christ, K. B. Williamson, K. S. Masters and K. T. Turner, Measurement of single-cell adhesion strength using a microfluidic assay. *Biomed Microdevices* **12**, 443–455 (2010).

[15] P. A. Coghill, E. K. Kesselhuth, E. A. Shimp, D. B. Khismatullin and D. W. Schmidtke, Effects of microfluidic channel geometry on leukocyte rolling assays. *Biomed Microdevices* **15**, 183–193 (2013).

[16] G. Coupier, B. Kaoui, T. Podgorski and C. Misbah, Noninertial lateral migration of vesicles in bounded Poiseuille flow. *Phys. Fluids* **20**, 11702 (2008).

[17] G. Coupier, A. Farutin, C. Minetti, T. Podgorski and C. Misbah, Shape Diagram of Vesicles in Poiseuille Flow. *Phys. Rev. Lett.* **108**, 178106 (2012).

[18] C. Couzon, A. Duperray and C. Verdier, Critical stresses for cancer cell detachment in microchannels. *Eur Biophys J* **38**, 1035–1047 (2010).

[19] B. Das, P. C. Johnson and A. S. Popel, Computational fluid dynamic studies of leukocyte adhesion effects on non-Newtoninan blood flow through microvessles. *Biorheology* **37**, 239-258 (2000).

[20] P. Dimitrakopoulos, Interfacial dynamics in Stokes flow via a three-dimensional fully-implicit interfacial spectral boundary element algorithm. *J. Comput. Phys.* **225**, 408-426 (2007).

[21] P. Dimitrakopoulos, Analysis of the variation in the determination of the shear modulus of the erythrocyte membrane: Effects of the constitutive law and membrane modeling. *Phys. Rev. E* **85**, 041917 (2012).

[22] S. K. Doddi and P. Bahci, Lateral migration of a capsule in a plane Poiseuille flow in a channel. *Int. J. Multiphase Flow* **34**, 966–986 (2008).

[23] W. R. Dodson III and P. Dimitrakopoulos, Dynamics of strain-hardening and strain-softening capsules in strong planar extensional flows via an interfacial spectral boundary element algorithm for elastic membranes. *J. Fluid Mech.* **641**, 263–296 (2009).

[24] C. Dong, J. Cao, E. J. Struble and H. H. Lipowsky, Mechanics of leukocyte deformation and adhesion to endothelium in shear flow. *Ann. Biomed. Eng.* **27**, 298–312 (1999).

[25] D. A. Fedosov, H. Lei, B. Caswell, S. Suresh and G. E. Karniadakis, Multiscale modeling of red blood cell mechanics and blood flow in malaria. *PLoS Comput. Biol.* **7**, e1002270 (2011).

[26] L. K. Fiddes, E. W. K. Young, E. Kumacheva and A. R. Wheeler, Flow of microgel capsules through topographically patterned microchannels. *Lab on a chip* **7**, 863–867 (2007).

[27] J. B. Freund, Leukocyte margination in a model microvessel. *Phys. Fluids* **18**, 023301 (2007).

[28] D. P. Gaver and S. M Kute, A theoretical model study of the influence of fluid stresses on a cell adhering to a microchannel wall. *Biophys. J.* **75**, 721–733 (1998).

[29] S. Hénon, G. Lenormand, A. Richert, and F. Gallet, A new determination of the shear modulus of the human erythrocyte membrane using optical tweezers. *Biophys. J.* **76**, 1145–1151 (1999).

[30] B. P. Ho and L. G. Leal, The creeping motion of liquid drops through a circular tube of comparable diameter. *J. Fluid Mech.* **71(2)**, 361–383 (1975).

[31] M. Husmann, H. Rehage, E. Dheninbursting of nonspherical polysiloxane microcapsules in a spinning-drop apparatus. *J. Colloid Interface Sci.* **282**, 109–119 (2005).

[32] A. H. G. Isfahani and J. B. Freund, Forces on a wall-bound leukocyte in a small vessel due to red cells in the blood stream. *Biophysics J.* **103**, 1604–1615 (2012).

[33] K. Jiang, P. C. Thomas, S. P. Forry, D. L. DeVoe and S. R. Raghavan, Microfluidic synthesis of monodisperse PDMS microbeads as discrete oxygen sensors. *Soft Matter* **8**, 923–926 (2012).

[34] B. Kaoui, G. H. Ristow, I. Cantat, C. Misbah and W. Zimmermann, Lateral migration of a two-dimensional vesicle in unbounded Poiseuille flow. *Phy. Rev. E.* **77**, 021903 (2008).

[35] D. B. Khismatullin and G. A. Truskey, Leukocyte rolling on P-selectin: A three-dimensional numerical study of the effect of cytoplasmic viscosity. *Biophysics J.* **102**, 1757–1766 (2012).

[36] S. M. Kim, S. H. Lee and K. Y. Suh, Cell research with physically modified microfluidic channel: A review. *Lab Chip* **8**, 1015–1023 (2008).

[37] S. Kuriakose and P.Dimitrakopoulos, Motion of an elastic capsule in a square microfluidic channel. *Phy. Rev. E* **84**, 011906 (2011).

[38] S. Kuriakose and P.Dimitrakopoulos, Deformation of an elastic capsule in a rectangular microfluidic channel. *Soft Matter* **9**, 4284–4296 (2013).

[39] E. Lac, D. Barthès-Biesel, N. A. Pelekasis and J. Tsamopoulos, Spherical capsules in three-dimensional unbounded Stokes flows: effect of the membrane constitutive law and onset of buckling, *J. Fluid Mech.* **516**, 303–334 (2004).

[40] E. Lac and D. Barthès-Biesel, Deformation of a capsule in simple shear flow: Effect of membrane prestress. *Phys. Fulids* **17**, 072105 (2005).

[41] E. Lac and J. D. Sherwood, Motion of a drop along the centreline of a capillary in a pressure-drive flow. *J. Fluid Mech.* **640**, 27–54 (2009).

[42] E. Leclerc, H. Kinoshita, T. Fujii and D. Barthès-Biesel , Transient flow of microcapsules through convergent-divergent microchannels. *Microfluid Nanofluid* **12**, 761–770 (2012).

[43] Y. Lefebvre and D. Barthès-Biesel, Motion of a capsule in a cylindrical tube : effect of membrane pre-stress. *J. Fluid Mech.* **589**, 157–181 (2007).

[44] Y. Lefebvre, E. Leclerc, D. Barthès-Biesel, J. Walter, and F. Edwards-Levy, Flow of artificial microcapsules in microfluidic channels: A method for determining the elastic properties of the membrane. *J. Fluid Mech.* **20**, 123102 (2008).

[45] A. Leyrat-Maurin and D. Barthès-Biesel, Motion of a deformable capsule through a hyperbolic constriction. *J. Fluid Mech.* **279**, 135–163 (1994).

[46] W. Mao and A. Alexeev, Hydrodynamic sorting of microparticles by size in ridged microchannels. *Phys. Fluids* **23**, 051704 (2011).

[47] F. Moazzam, F. A. Delano, B. W. Zweifach and G. W. Schmid-Schönbein, The leukocyte response to fluid stress. *Proc. Natl. Acad. Sci. USA* **94**, 5338–5343 (1997).

[48] N. Mohandas and J. A. Chasis, Red blood cell deformability, membrane material properties and shape: regulation by transmembrane, skeletal and cytosolic proteins and lipids. *Semin. Hematol.* **30**, 171–192 (1993).

[49] H. Noguchi and G. Gompper, Shape transitions of fluid vesicles and red blood cells in capillary flows. *Proc. Natl. Acad. Sci. USA* **102(40)**, 14159–14164 (2005).

[50] H. Noguchi, G. Gompper, L. Schmid, A.Wixforth and T. Franke, Dynamics of fluid vesicles in flow through structured microchannels. *Europhys. Lett.* **89**, 28002 (2010).

[51] W. L. Olbricht and L. G. Leal, The creeping motion of immiscible drops through a converging/diverging tube. *J. Fluid Mech.* **134**, 329–355 (1983).

[52] V. Pappu, S. K. Doddi and P. Bagchi, A computational study of leukocyte adhesion and its effect on flow pattern in microvessels. *Journal of Theoretical Biology* **254**, 483–498 (2008).

[53] S. Y. Park and P. Dimitrakopoulos, Transient dynamics of an elastic capsule in a microfluidic constriction. *Soft Matter under review* (2013)

[54] J. E. Pickard and Klaus Ley, Micro-PTV measurement of the fluid shear stress acting on adherent leukocytes in vivo. *Biophysical Journal* **96(10)**, 4249–4259 (2009).

[55] A. S. Popel and P. C. Johnson, Microcirculation and hemorheology. *Annu. Rev. Fluid Mech.* **37**, 43–69 (2005).

[56] C. Pozrikidis, Shear flow over a protuberance on a plane wall. *Journal of Engineering Mathematics* **31**, 29–42 (1997).

[57] C. Pozrikidis, Effect of pressure gradient on viscous shear flow past an axisymmetric depression or protuberance on a plane wall *Computer & Fluids* **29**, 617–637 (2000).

[58] C. Pozrikidis, *Modeling and Simulation of Capsules and Biological Cells*. Chapman and Hall/CRC (2003).

[59] C. Pozrikidis, Axisymmetric motion of a file of red blood cells through capillaries. *Phys. Fluids* **17**, 031503 (2005).

[60] C. Pozrikidis, Particle motion near and inside an interface. *J. Fluid Mech.* **575**, 333–357 (2007).

[61] M. Prevot, A. L. Cordeiro, G. B. Sukhorukov, Y. Lvov, R. S. Besser and H. Mohwald, Design of a microfluidic system to investigate the mechanical properties of layer-bylayer fabricated capsules. *Macromol. Mater. Eng.* **288**, 915–919 (2003).

[62] C. Quèguiner and D. Barthès-Biesel, Axisymmetric motion of capsules through cylindrical channels. *J. Fluid Mech.* **348**, 349–376 (1997).

[63] F. Risso, F. Collé-Paillot and M. Zagzoule, Experimental investigation of a bioartificial capsule flowing in a narrow tube. *J. Fluid Mech.* **547**, 149–173 (2006).

[64] T. W. Secomb, R. Hsu and A. R. Pries, Blood flow and red blood cell deformation in nonuniform capillaries: effects of the endothelial surface layer. *Microcirc.* **9**, 189–196 (2002).

[65] S. Seiffert, J. Thiele, A. R. Abate and D. A. Weitz, Smart microgel capsules from macromolecular precursors. *J. Am. Chem. Soc.* **132**, 6606–6609 (2010).

[66] A. Sequeiraa, A.M. Artolia, A.S. Silva-Herdadeb and C. Saldanhab, Leukocytes dynamics in microcirculation under shear-thinning blood flow. *Computers and Mathematics with Applications* **58**, 1035–1044 (2009).

[67] S. She, C. Xu, X. Yin, W. Tong and C. Gao, Shape deformation and recovery of multilayer microcapsules after being squeezed through a microchannel. *Langmuir* **28(11)**, 5010–5016 (2012).

[68] J. P. Shelby, J. White, K. Ganesan, P. K. Rathod, and D. T. Chiu, A microfluidic model for single-cell capillary obstruction by Plasmodium falciparum infected erythrocytes. *Proc. Natl. Acad. Sci. USA* **100**, 14618–14622 (2003).

[69] R. Skalak and P. I. Branemark, Deformation of red blood cells in capillaries. *Science* **164**, 717–719 (1969).

[70] R. Skalak, A. Tozeren, R. P. Zarda and S. Chien, Strain energy function of red blood cell membranes. *Biophys. J.* **13(3)**, 245–264 (1973).

[71] R. Skalak, N. Özkaya and T. C. Skalak, Biofluid Mechanics. *Annu. Rev. Fluid Mech.* **21**, 167–204 (1989).

[72] M. Sugihara-Seki and G. W. Schmid-Schönbein, The fluid shear stress distribution on the membrane of leukocytes in the microcirculation. *J. Biomech. Eng.* **125(5)**, 628–638 (2003).

[73] C. Sun and L. L. Munn, Particulate nature of blood determines macroscopic rheology: A 2-D lattice Boltzmann analysis. *Biophys. J.* **88**, 1635–1645 (2005).

[74] G. Tomaiuolo, M. Simeone, V. Martinelli, B. Rotolib and S. Guido, Red blood cell deformation in microconfined flow. *Soft Matt* **5**, 3736–3740 (2009).

[75] O. B. Usta, M. Nayhouse, A. Alexeev and A. C. Balazs, Designing patterned substrates to regulate the movement of capsules in microchannels. *J. Chem. Phys.* **128**, 235102 (2008).

[76] Y. Wang and P. Dimitrakopoulos, A three-dimensional spectral boundary element algorithm for interfacial dynamics in Stokes flow. *Phys. Fluids* **18**, 082106 (2006).

[77] Y. Wang and P. Dimitrakopoulos, Nature of the hemodynamic forces exerted on vascular endothelial cells or leukocytes adhering to the surface of blood vessels. *Phys. Fluids* **18**, 087107 (2006).

[78] Y. Wang and P. Dimitrakopoulos, Normal force exerted on vascular endothelial cells. *Phys. Rev. Lett.* **96**, 028106 (2006).

[79] C. -S. Yih, *Fluid Mechanics*. West River Press, Ann Arbor (1979).

[80] G. Zhu, A. Alexeev and A. C. Balazs, Designing constricted microchannels to selectively entrap soft particles. *Macromolecules* **40**, 5176–5181 (2007).

[81] G. Zhu, A. Alexeev, E. Kumacheva and A. C. Balazs, Modeling the interactions between compliant microcapsules and pillars in microchannels. *J. Chem. Phys.* **127**, 034703 (2007).

Vita

Sun-Young Park was born in Seoul, South Korea. She entered the Department of Chemical Engineering at the University of Seoul at Seoul, South Korea in March 2003. She graduated in February 2007 receiving her Bachelor of Science degree in Chemical Engineering. After receiving her Bachelor's degree, she enrolled for graduated studies at the Department of Chemical Engineering at the University of Seoul at Seoul, South Korea, in September 2007. She investigated numerically the fluid dynamics at the high-Reynolds-number flows. In June 2009, she graduated and received a Masters of Science degree. Her master thesis was titled "Nonlinear dynamics of a high Reynolds-number film flow under an electrostatic field". Sun-Young Park joined the graduate program of the Department of Chemical and Biomolecular Engineering at the University of Maryland at College Park in September 2009. In January 2010, she joined the Bio-Fluid Dynamics Laboratory and conducted research on the flow dynamics of capsules in microfluidic constricted channels under the guidance of Professor Panagiotis Dimitrakopoulos. In June 2013, she is defending her dissertation for the Doctor of Philosophy degree, entitled "Dynamics of elastic capsules in constricted microfluidic channels".